Thesis for the degree of Licentiate of Engineering

Modelling of wheel/rail interaction considering roughness and discrete irregularities

Astrid Pieringer

Department of Civil and Environmental Engineering
Division of Applied Acoustics, Vibroacoustic Group
Chalmers University of Technology
Göteborg, Sweden, 2008

Modelling of wheel/rail interaction considering roughness and discrete irregularities

Astrid Pieringer

Technical report: lic 2008:10
ISSN 1652-9146

Department of Civil and Environmental Engineering
Division of Applied Acoustics, Vibroacoustic Group
Chalmers University of Technology
SE-412 96 Göteborg, Sweden
Telephone + 46 (0) 31-772 2200

Printed by
Chalmers Reproservice
Göteborg, Sweden, 2008

Modelling of wheel/rail interaction considering roughness and discrete irregularities

Astrid Pieringer

Department of Civil and Environmental Engineering
Division of Applied Acoustics, Vibroacoustic Group
Chalmers University of Technology

Abstract

The interaction between wheel and rail is the predominant source of noise emission from railway operations in a wide range of conventional speeds. On the one hand, this wheel/rail noise concerns rolling noise and impact noise caused by the vertical interaction excited by roughness and discrete irregularities of the wheel/rail running surfaces, respectively. On the other hand, it concerns squeal noise generated by the tangential interaction. While a well-established frequency-domain model is available for the prediction of rolling noise, likewise successful models do not yet exist for the prediction of impact noise and squeal noise. The overall aim of this thesis is to develop a model for the vertical wheel/rail interaction induced by roughness and discrete irregularities. The inclusion of tangential interaction is a subject of future work.

In order to include the non-linearities in the contact zone, the interaction model presented in this thesis is formulated in the time domain. Wheel and track models are represented by Green's functions, which leads to a computationally efficient formulation and allows inclusion of detailed non-Hertzian contact models. The first contact model considered is a two-dimensional (2D) model consisting of a bedding of independent springs. This model uses a simplified wheel and rail geometry and takes into account one line of wheel/rail roughness in the rolling direction. The second contact model is a three-dimensional (3D) model based on an influence-function method for the elastic half-space. This model considers the real three-dimensional wheel and rail geometry and includes the roughness in several parallel lines.

In the thesis, the interaction model using both the 2D and the 3D contact models is applied to simulate the wheel/rail interaction caused by parametric excitation on a discretely supported rail and by wheel/rail roughness. The results indicate that the application of the 3D contact model is preferable when the degree of correlation between roughness across the width of the contact is low, although more simulations should be carried out before drawing a final conclusion. The interaction model using the 2D contact model is applied to simulate impact forces caused by wheel flats and shows encouraging agreement with field measurements.

Keywords: vertical wheel/rail interaction, time domain, non-Hertzian contact, roughness, discrete irregularities, railway noise.

List of publications

This thesis is based on an extended summary and the following appended papers, referred to by Roman numerals in the text:

Paper I
A. Pieringer, W. Kropp and J.C.O. Nielsen.
A time domain model for wheel/rail interaction aiming to include non-linear contact stiffness and tangential friction.
Proceedings of the Ninth International Workshop on Railway Noise (9th IWRN), Munich, Germany, September 4-8, 2007.

Paper II
A. Pieringer and W. Kropp.
A fast time-domain model for wheel/rail interaction demonstrated for the case of impact forces caused by wheel flats.
Proceedings of Acoustics'08, Paris, France, June 29-July 4, 2008.

The following paper is a short version of *Paper I* and is therefore not included in the thesis:

A. Pieringer, W. Kropp and J.C.O. Nielsen.
A time domain model for wheel/rail interaction aiming to include non-linear contact stiffness and tangential friction.
In B. Schulte-Werning et al. (Eds.), *Noise and Vibration Mitigation for Rail Transport Systems*, NNFM 99, pp. 285-291, Springer-Verlag, Berlin Heidelberg, 2008.

Acknowledgements

The work described in this thesis has been carried out during the years 2006-2008 at the Division of Applied Acoustics at Chalmers University of Technology within the project “Generation of External Noise from Trains” (VB10). The project forms part of the activities in the Centre of Excellence CHARMEC (CHAlmers Railway MEChanics). The project is partly funded by VINNOVA (the Swedish Governmental Agency for Innovation Systems) under contract no 27465-1.

First and foremost, I would like to express my deepest gratitude to my supervisor Professor Wolfgang Kropp, who gives me both the guidance and the leeway I need and never stops encouraging me. Special thanks to Jannick for sleeping so well on his father’s arm and making available extra supervision time. I would also like to thank my assistant supervisor Dr. Anders Frid from Bombardier Transportation Sweden, Västerås, for valuable advice and interesting discussions.

I am especially grateful to Professor Jens Nielsen for giving me access to his program DIFF and to measurement data, and for the great advice and help I received in the various areas of wheel/rail interaction. I would like to thank Peter Torstensson in the joint project TS11 for fruitful and pleasant cooperation and for giving me the opportunity to take part in his measurement campaign. I am grateful to SL for permitting roughness measurements on their network, to Fredrik Jansson (Banverket) for carrying out the measurements during Stockholm’s cold nights and to the staff from Strukton Rail for their practical help. The contribution of the reference group members Roger Deuce (Bombardier Transportation GmbH), Mats Knutsson (SL), Rickard Nilsson (SL), Nicolas Renard (Banverket), Philipp Ruest (Bombardier Transportation Switzerland) to the project is greatly acknowledged.

I feel privileged to work at such a nice place as Applied Acoustics and would like to thank all the people at the Division contributing to the open-minded and friendly atmosphere. Many thanks go to Gunilla Skog and Börje Wijk for uncomplicated and effective help in administrative and technical matters, to my colleagues for unforgettable common activities such as the annual Midsummer celebration and to my room mate Jonas Svensson for making daily office life very enjoyable.

Last but not least, *tusen takk*, Stig, for your invaluable support, for accepting long working hours and for reminding me all the other important things in life.

Contents

Chapter 1
Introduction

1.1 Background

Railways are generally considered to be a more environmentally friendly means of transportation than aircraft and road traffic. Noise is one of their few environmental drawbacks. Although exposure to noise from railways is experienced by many as less disturbing than noise from aircraft and road traffic at the same sound level [12, 36], it is still a source of considerable annoyance for residents in the vicinity of railway lines.

Railway noise is generated by diverse sources, whose relative relevance depends on the operating conditions. The importance of noise from the power unit and auxiliaries is confined to standstill, acceleration and low speeds below about $60\,\mathrm{km/h}$ [11]. For high-speed operation above approximately $300\,\mathrm{km/h}$, aerodynamic noise becomes dominant. This type of noise is generated by unsteady airflow over structural elements such as the bogies and the pantograph and by the turbulent boundary layer [14].

In the wide range of conventional speeds in between, the interaction between wheel and rail is the predominant source of noise emission. This wheel/rail noise is divided into the three categories of rolling noise, impact noise and squeal noise. While the former two are caused by the vertical wheel/rail interaction, the latter is induced by a lateral excitation mechanism [67]. Rolling noise is generated by the roughness of the wheel and rail running surfaces, which excites vibrations of track and wheel in the form of a vertical relative motion. In consequence, the wheelset, the rail and the sleepers radiate noise [67]. The vehicle superstructure comprising cars and bogies does not contribute significantly to the radiation of rolling noise [14]. Impact noise is caused by discrete irregularities of the wheel and rail running surfaces such as wheel flats and rail joints. The underlying mechanism can be interpreted as an extreme form of roughness excitation [67]. Squeal noise occurring in sharp curves is generated by lateral forces due to frictional instability. While rolling noise and also impact noise are broad-band phenomena involving a large range of frequencies in the audible range, squeal noise is generally a tonal sound that dominates all other types of noise when it occurs. Summing up, it can

be said that all three types of wheel/rail noise have their origin in the contact zone between wheel and rail. The dynamic processes occurring in this area, which is generally not bigger than a one-cent coin for a steel wheel on a steel rail, are of great importance for the generation of wheel/rail noise.

Traffic operators, infrastructure administrators, train manufacturers and society in general all have an interest in the reduction of wheel/rail noise. Computer models that increase the physical understanding of the noise generation process and allow to assess possible noise reduction measures can assist in fulfilling this aim. A good example is the frequency-domain model TWINS developed for the prediction of rolling noise [66]. This model is widely used today in industry and has been applied extensively in the identification and assessment of measures to reduce rolling noise [65]. Corresponding models for the prediction of impact noise and squeal noise that would be as successful as TWINS are not yet available. One of the difficulties is that wheel/rail interaction models aiming to predict these types of noise have to be formulated in the time domain and are generally computationally demanding.

1.2 Overall aim

Owing to the fact that the development of a combined prediction model for rolling noise, impact noise and squeal noise is a complex task, the work in this thesis is limited to the vertical wheel/rail interaction. First, this implies that the formulation of a radiation and sound propagation model is not included in the scope of this thesis. The results of the developed wheel/rail interaction model can however be used as input to existing models such as TWINS in order to predict rolling and impact noise [72]. A second implication is that squealing and tangential interaction are not addressed in this thesis. It is nevertheless intended to include tangential interaction in the future as a continuation of the presented work.

Accordingly, the overall aim of the work presented in this thesis is to develop a model for the vertical wheel/rail interaction induced by the roughness and discrete irregularities of the wheel/rail running surfaces.

1.3 Outline

The general structure of the thesis is as follows.

Chapter 2 provides a literature review on wheel/rail interaction models. This review serves to define the various requirements on the vertical wheel/rail interaction model developed in this thesis and to motivate the choices made in the modelling process.

The resulting wheel/rail interaction model with all its components is elaborated in *Chapter 3*. In particular, two different non-Hertzian contact models are introduced.

Chapter 4 presents simulation results of the interaction model. First, two specific areas of application are treated. These are the evaluation of the contact-filter effect consisting in the suppression of short wavelength excitation by the finite size of the contact area, and the calculation of impact forces caused by wheel flats. Secondly, a comparison is carried out between the two contact models.

The appended papers, *Paper I* and *Paper II*, contain additional simulation results in the mentioned areas of application and also provide a validation of the interaction model against an existing model and field measurements.

Chapter 2

Review of the modelling of wheel/rail interaction

2.1 Modelling concepts

Wheel/rail interaction models intended for noise prediction should cover the frequency range from approximately $100\,\mathrm{Hz}$ to $5\,\mathrm{kHz}$. At frequencies below $100\,\mathrm{Hz}$ the human perception of sound is substantially reduced. Due to the contact-filter effect (described in *Section 2.2*) the rolling noise spectrum decreases rapidly above $5\,\mathrm{kHz}$ [68]. Such wheel/rail interaction models are denoted high-frequency models to distinguish them from models of the classical rail-vehicle dynamics considering for instance running stability, curving behaviour and passenger comfort, which typically include frequencies up to $20\,\mathrm{Hz}$ [30].

The purpose of a wheel/rail interaction model is to calculate the response of the vehicle/track system to an excitation acting in the contact zone. Typical input variables are the combined roughness of wheel and rail or the shape of a discrete irregularity. Typical output variables are the vibrations of vehicle and track and the contact forces acting at the interface.

In general, wheel/rail interaction models consist of three subsystems: a vehicle model, a track model and a contact model; see Figure 2.1. The vehicle and track model describe the global dynamics of the vehicle and the track. They are coupled via the contact model, which comprises the local dynamics in and close to the contact zone of wheel and rail.

The interaction of wheel and rail can be summarised as follows. When the wheel rolls over the rail, the roughness or the discrete irregularity (seen as rigid indenter) causes a relative vertical displacement between wheel and rail [58]. This relative displacement is partly taken up by local deformation in the contact zone and is partly transformed into global vibrations of vehicle and track. The proportion of local deformation and global vibrations is determined by the dynamic properties of the vehicle, the track and the contact zone. The local deformation in the contact zone involves a varying contact pressure distribution, which is often represented as a point force - the contact force.

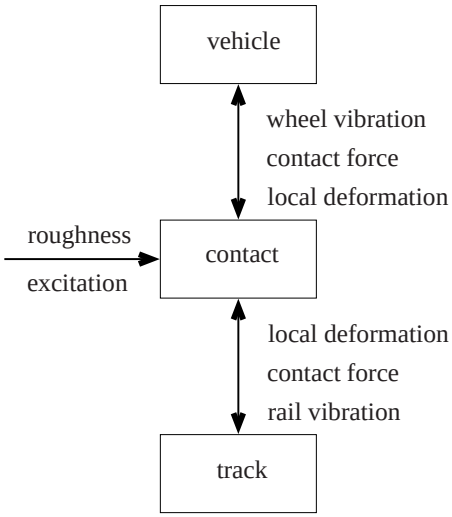

Figure 2.1: Schematic sketch of a wheel/rail interaction model.

Wheel/rail interaction models can be formulated either in the frequency or in the time domain. By their nature, frequency-domain models are completely linear models, while time-domain models are suitable to include all kind of non-linearities. A disadvantage of time-domain models is that they are generally more computationally demanding than are frequency-domain models.

Frequency-domain models work with frequency response functions such as receptances or impedances that represent the dynamic behaviour of the vehicle, the track and the contact zone. It is implicitly assumed that a roughness component of wavelength λ, which is passed by the wheel at train speed v, excites the wheel/rail system at the frequency

$$f = \frac{v}{\lambda} \tag{2.1}$$

and causes vibrations only at this frequency f.

A considerable number of frequency-domain models for wheel/rail interaction is available in the literature, e.g. [15, 21, 35, 43, 49–52, 56, 58–62], and a good overview of these models is given in the review article of Knothe and Grassie [30]. The most well known frequency-domain model for the calculation of rolling noise is a model going back to Remington [49–52], which has been generalised and further improved by Thompson [58–62]. His formulation is implemented in the software package TWINS [68] which is widely used in industry today. Two basic equations of Thompson's model, which are repeated here for vertical coupling between the wheel and the rail only, illustrate well the functioning of wheel/rail

interaction models in the frequency domain:

$$\Xi_{\mathrm{W}} = \frac{-G_{\mathrm{W}}R}{G_{\mathrm{W}}+G_{\mathrm{R}}+G_{\mathrm{C}}} \tag{2.2}$$

$$\Xi_{\mathrm{R}} = \frac{G_{\mathrm{R}}R}{G_{\mathrm{W}}+G_{\mathrm{R}}+G_{\mathrm{C}}}\,. \tag{2.3}$$

The vibration amplitude of the wheel, Ξ_{W}, and of the rail, Ξ_{R}, at a certain frequency due to a roughness component with amplitude R, is determined by the receptance of the wheel, G_{W}, the rail, G_{R} , and the contact zone, G_{C}.

The range of validity of the assumption of linearity that is necessary in frequency-domain models has been investigated by Wu and Thompson [71] using a time-domain model. They found that non-linearities in the contact model cannot be neglected in the cases of severe roughness and/or a low static contact preload, which can cause loss of contact between wheel and rail. These results have been confirmed by Nordborg who used both a frequency-domain model and a time-domain model based on Green's functions to study non-linear effects in the vertical interaction [43]. If the response to discrete irregularities such as wheel flats and rail joints is to be calculated, time-domain models are the only option. Only they can capture the discrete nature of the phenomena and model the loss of contact that is likely to occur [72, 73].

Time-domain models essentially solve the system of differential and algebraic equations describing vehicle, track and contact by a time-stepping procedure. A common approach is to model the track as a modal component derived from a finite-element model, e.g. [9, 41], but such models have generally long calculation times [30]. An alternative, more computationally efficient approach has been demonstrated by Wu and Thompson [72]. They modelled the dynamics of the track using a single differential equation obtained from a transfer function $H(s)$

$$H(s) = \frac{b_1 s^3 + b_2 s^2 + b_3 s + b_4}{s^4 + a_1 s^3 + a_2 s^2 + a_3 s + a_4} \tag{2.4}$$

whose constant coefficients a_i and b_i were adapted in such a way that the differences between $H(\mathrm{i}\omega)$ and the point receptance of the track were minimised. Their technique is, however, not suitable to include track models with discrete supports. A third, very promising, approach that is computationally efficient and allows including discrete supports is the representation of the track by moving Green's functions that describe the dynamic behaviour of the track in a moving contact point. This technique going back to Heckl's proposal for a railway simulation program [20], has e.g. been used by Nordborg [43] and recently by Mazilu [34].

2.2 Excitation by roughness

It is now generally accepted that the roughness of wheel and rail running surfaces is the predominant cause of the occurrence of rolling noise [67]. Applying Equation (2.1) for the frequency range of interest from $100\,\mathrm{Hz}$ to $5\mathrm{kHz}$ and train speeds ranging from 50 to $300\,\mathrm{km/h}$ leads to a relevant roughness-wavelength interval from 830 to $3\,\mathrm{mm}$. Thompson [63] estimates that the wavelength range $300 - 10\,\mathrm{mm}$ is the most important. Typical roughness amplitudes are in the range $0.1 - 30\,\mu\mathrm{m}$. For severely corrugated rail, even higher amplitudes occur [63].

Wheel and rail make contact not only in a point, but in a small area denoted a contact patch. The roughness distribution throughout this contact patch is responsible for the excitation of vibrations. Nevertheless, most available wheel/rail interaction models - including all models mentioned in *Section 2.1* except Heckl's proposal [20] - assume that the roughness distribution effectively acts in one point. This implicitly includes the assumption that the contact-patch size and shape are not influenced by the roughness.

The finite size of the contact patch is responsible for two important effects concerning the excitation of the wheel/rail system by roughness [63]:

1. Roughness components of wavelengths that are in the order of or shorter than the length of the contact zone in the rolling direction do not excite the system as effectively as roughness components of longer wavelengths, an effect known as the contact-filter effect.

2. The excitation of the wheel/rail system depends also on the variations in roughness profile height across the width of the contact in lateral direction. The excitation is greatest when the roughness is strongly correlated across the contact patch and progressively decreases as the roughness becomes uncorrelated.

Models which assume that the roughness distribution effectively acts in one point have to account for these two effects by roughness pre-processing. In frequency domain models, this is done by adding a correction - the contact filter - to the roughness spectrum (in dB). Remington [51] proposed an analytical model of such a contact filter for circular contact patches of radius a

$$|H(k)|^2 = \frac{4}{\alpha}\frac{1}{[ka]^2}\int_0^{tan^{-1}\alpha} [J_1(ka\,\sec\chi)]^2\,\mathrm{d}\chi\,, \tag{2.5}$$

which gives the correction $|H(k)|$ as a function of the roughness wavenumber $k = [2\pi]/\lambda$, λ being the wavelength. The function J_1 is the Bessel function of order 1 and the parameter α is a measure of the degree of correlation between roughness across the width of the contact, where a small value of α implies a high

degree of correlation.

More recently, Remington and Webb [48] presented a contact model based on a three-dimensional bedding of independent springs, which allows considering the actual roughness distribution in the contact patch and thereby includes effects 1 and 2 above in a natural manner. They called their model a three-dimensional 'distributed point reacting spring' (3D-DPRS) model. Thompson [64] applied this model to calculate numerical frequency-domain contact filters from roughness data measured in several parallel lines. He concluded that the analytical contact filter of Equation (2.5) gives an attenuation that is too large at short wavelengths, but gives reasonable results for wavelengths down to somewhat smaller than the contact-patch length if the right value of α is chosen. The discrepancies at short wavelengths are attributed to the fact that the 3D-DPRS model, in contrast to the analytical model, takes account of the variation of the normal load across the contact patch. As in many practical cases, only one line of roughness is measured, Ford and Thompson [13] developed a two-dimensional version of the DPRS model which they found to perform surprisingly well in comparison to the 3D-DPRS model. The 2D-DPRS model, however, cannot consider correlation effects across the contact width, which explains differences of a few dB between both models at wavelengths as short as the contact patch length or shorter.

To include the contact-filter effect in time-domain models, one possibility is to calculate an equivalent roughness as a pre-processing step, which represents the roughness distribution experienced by the system for each wheel position on the rail. The 2D-DPRS model [13] (or even the 3D-DPRS model if the required roughness data are available) can be applied for this task. A simpler but less accurate means to obtain an equivalent roughness is to calculate an average of the roughness over the nominal contact patch length (which is the length in the absence of roughness) [13]. Another possibility making unnecessary the mentioned roughness pre-processing is to directly consider the finite size of the contact patch at each time step in a wheel/rail interaction model, by using an appropriate contact model. Ford and Thompson implemented the 2D-DPRS model as a contact model in a time-domain model and presented some preliminary results [13].

2.3 Excitation by discrete irregularities

The most common discrete irregularities that are responsible for the occurrence of impact noise are wheel flats and rail joints. A wheel flat is a defect of the running surface of a railway wheel that occurs when the wheel locks and slides along the rail because of malfunction in the brakes or lack of wheel/rail adhesion. The sliding causes severe wear, leading to the wheel being flattened on one side [23]. At a rail

joint, the rail running surface shows a severe discontinuity characterised by a gap and a height difference between the two sides of the gap. Moreover, the rail often dips close to a joint [73].

In wheel/rail interaction models, discrete irregularities are generally introduced as a form of extreme roughness described by simple analytic functions. Newton and Clark [38] used for instance the following shape, $f(x)$, to represent a rounded wheel flat

$$f(x) = \frac{d}{2}\left[1 - \cos 2\pi \frac{x}{l}\right]; \quad d = \frac{l^2}{16r}, \tag{2.6}$$

where x is the distance along the flat, d the maximum depth of the wheel flat, l its length, and r the wheel radius. Similar descriptions of wheel flats have been used, amongst others, by Nielsen and Igeland [41], Mazilu [34] and Baeza et al. [5]. Wu and Thompson [73] proposed quadratic functions to describe the dipped rail at a joint.

In a similar manner as for roughness excitation, models with one effective contact point have to take into account how the wheel/rail system effectively "sees" the discrete irregularity. Due to its finite curvature, the wheel does not follow the irregularity shape as described, for example, by Equation (2.6). Wu and Thompson included this effect by calculating equivalent irregularity shapes for wheel flats [72] and rail joints [73]. Baeza et al. used the same equivalent irregularity shape for wheel flats [5]. Additionally, they included the changes in stiffness due to the wheel flat geometry by pre-calculating stiffness functions for each angular position of the wheel flat with a three-dimensional contact model. An alternative way to account for the changes in the contact zone and the finite curvature of the wheel would again be to incorporate an appropriate contact model that is evaluated at each step in a time-domain model, though this seems not to have been done yet.

2.4 Vehicle and track models

Vehicle models in vertical high-frequency wheel/rail interaction models are generally simple. As the vehicle's primary and secondary suspensions isolate the bogie and car body from the wheelset at frequencies of more than a few Hertz, the vehicle's dynamic behaviour in the interaction model is sufficiently described by the dynamics of the wheelset [30]. Knothe and Grassie [30] state that the vehicle's unsprung mass (including wheelset, bearings and axle-mounted components) is even satisfactorily represented as a rigid body for vertical interaction. If however lateral wheel/rail interaction is to be considered, more advanced wheel models are required, which include the wheel's flexibility [30].

In contrast to the situation for the wheel, sophisticated models are necessary to represent the track's dynamic behaviour in the frequency range of interest up to $5\,\mathrm{kHz}$.

Available track models are distinguished in their representation of the rail and the supports.

Historically, the rail has often been modelled as an Euler-Bernoulli beam, neglecting shear deformation and rotational inertia. Such simple beam models can only represent the track's vertical dynamics up to about $500\,\mathrm{Hz}$ [30]. Using a Timoshenko beam model for the rail, which includes rotational inertia and shear deformation, the frequency range of validity of the track model can be extended, the upper limit frequency being a subject of discussion. Knothe and Grassie [30] estimate that the rail can be modelled as a single Timoshenko beam up to $2.5\,\mathrm{kHz}$ if only vertical vibrations are of interest. Wu and Thompson [71] state that such models are adequate up to about $5\,\mathrm{kHz}$ since the occurring cross-sectional deformations of the rail (not modelled by Timoshenko-beam models) are not important in terms of the vertical wheel/rail interaction in this frequency range (see also [68, 69]). A Timoshenko beam model of the rail is for instance implemented in the wheel/rail interaction model DIFF developed by Nielsen and Igeland [41]. In order to include the cross-sectional deformations that become significant above about $1.5\,\mathrm{kHz}$ [60], different types of rail models are required. One example is the multi-layer model by Scholl [54], who represented rail head, web and foot by three infinitely long, homogeneous layers with different densities and Young's moduli. Vibrational shapes with cross-sectional deformation can at least in principle be modelled by this approach. A second example is the model by Thompson [60] who used a detailed finite-element mesh for a short length of the rail, which he extended to infinity using periodic structure theory. Gry [19] presented a third alternative model based on a description of waves travelling through the rail.

Concerning the supports, models with a continuous support of the rail and models with discrete supports are distinguished. Nordborg found that the inclusion of discrete supports is important for lower frequencies around the sleeper-passing frequency and for higher frequencies around the pinned-pinned resonance frequency of the rail [43]. The sleeper-passing frequency, $f_\mathrm{S} = v/L_\mathrm{S}$, is the frequency at which the wheelset passes the sleepers, v being the train speed and L_S the sleeper spacing. At the pinned-pinned frequency, f_p, which typically lies around $1\,\mathrm{kHz}$, the bending wavelength of the rail corresponds to the length of two sleeper spans, $\lambda_\mathrm{p} = 2L_\mathrm{S}$, with nodes located at the sleeper positions. Knothe and Grassie [30] give an overview of different ways to model supports comprising railpads, sleepers, ballast and substrate.

2.5 Hertzian model for normal contact

The normal[1] contact model applied in most of the available interaction models is the Hertzian contact model; see e.g. the models [34, 41, 43, 51, 66, 71]. This standard model goes back to Heinrich Hertz who published his theory "On the contact of elastic solids" already in 1882 [22]. A comprehensive description of the Hertzian contact theory can e.g. be found in [25] or [33]. In this section, only a short outline of the theory is given and the connection to the railway case is established, which provides a basis for the discussion of non-Hertzian models in *Section 2.6*.

The Hertzian theory of normal contact between two bodies relies on the following assumptions [25]

1. *Linear elasticity*
   The bodies are perfectly linear elastic solids.

2. *Half-space assumption*
   The surfaces of the bodies are non-conforming surfaces, i.e. they first make contact at a point (or along a line). Even under load, the dimensions of the contact area are small in comparison to the dimensions of the bodies and the radii of curvature of the surfaces. This implies that the bodies can be considered as a semi-infinite elastic solid with a plane surface (an elastic half-space) for the purpose of stress and deformation calculations.

3. *Smoothness*
   The surfaces are perfectly smooth.

4. *Hertzian surfaces*
   The surfaces can be described by quadratic functions in the vicinity of the contact area (see below).

5. *Absence of friction*
   No friction occurs in the contact area. Only normal pressure is transmitted.

Under these assumptions, the contact area is an ellipse and the normal pressure distribution is ellipsoidal. The case of contact over a long strip as it occurs for two cylindrical bodies with their axes lying parallel is a limit case of elliptical contact. This case has to be treated separately and is not further considered here. The following presentation of the relevant formulas for contact dimensions, loads and deformations in elliptical contact mainly follows the presentation by Lundberg and Sjövall [33].

[1] The denotation ‘normal’ is here used in the sense ‘in the direction normal to the surfaces of rail and wheel’. As the difference between the normal and the vertical direction is negligible in the case of tread contact, ‘normal’ and ‘vertical’ are used as synonyms throughout this thesis.

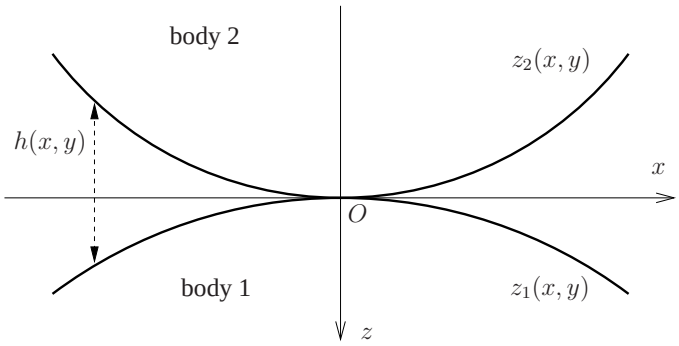

Figure 2.2: *Two non-conforming surfaces touching at the point O.*

Assume that two non-conforming surfaces as seen in Figure 2.2 are brought into contact without loading. They only touch in one point that is taken as origin O of a Cartesian coordinate system xyz. The xy-plane is the tangent plane to the surfaces at the origin, and the z-axis is the common normal to the two surfaces pointing into body 1. Under assumption 4, the surfaces of bodies 1 and 2 in the vicinity of the contact point are then described by

$$z_1(x_1, y_1) = \frac{x_1^2}{2r_{x_1}} + \frac{y_1^2}{2r_{y_1}} \tag{2.7}$$

$$z_2(x_2, y_2) = -\left(\frac{x_2^2}{2r_{x_2}} + \frac{y_2^2}{2r_{y_2}}\right), \tag{2.8}$$

where r_{x_1} and r_{y_1} are the principal radii of curvature of surface 1 at the origin, i.e. the minimum and maximum values of the radius of curvature of all possible cross-sections of the profile, which are found in perpendicular planes denoted the x_1z- and the y_1z-planes). The variables r_{x_2} and r_{y_2} are the principal radii of curvature of surface 2 at the origin, found in the x_2z- and y_2z-planes. Each radius of curvature is positive if the curvature centre is located inside the body (convex surface) and negative if the curvature centre is located outside (concave surface). The x_1z- and x_2z-planes enclose an angle ψ.

In the railway case, the wheel rolling radius, r_{x_2}, and the rail transverse radius of curvature, r_{y_1}, are generally positive, while the wheel transverse radius of curvature, r_{y_2}, can be positive or negative [4]. The rail radius in the rolling direction, r_{x_1}, is assumed infinite. The wheel and rail radii of curvature are determined at the geometric point of contact, which is the point $O = O_1 = O_2$ in Figure 2.3. The geometric point of contact depends on the wheel and rail profiles and the translatory and angular position of the wheel on the rail and is calculated for wheel and rail considered as rigid.

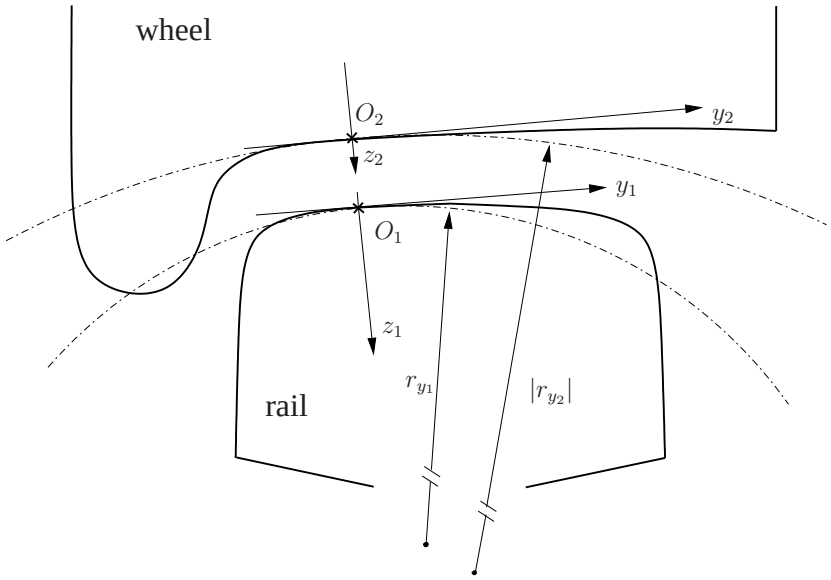

Figure 2.3: *Transverse radius of curvature of the rail, r_{y_1}, and the wheel, r_{y_2}, for contact occurring at O_1-O_2.*

Considering Equations (2.7) and (2.8), the distance of the undeformed surfaces can be expressed by

$$h(x,y) = \frac{x^2}{2r_x} + \frac{y^2}{2r_y}\,, \tag{2.9}$$

with suitable orientation of the x- and y-axes. The variables r_x and r_y denote the principal *relative* radii of curvature of the surfaces, which can be calculated from the principal radii of curvature of both surfaces, $r_{x_1}, r_{y_1}, r_{x_2}, r_{y_2}$, and the angle ψ [33].

When the two bodies are pressed together with a load P, they deform locally and the contact point develops into a contact ellipse with semi-axes a and b, where by definition $a > b$. Distant points in the two bodies approach by a distance δ. The ratio of the semi-axes of the contact ellipse, $A = a/b$, depends only on the relative principal radii of curvature, r_x and r_y.

The final equations for the semi-axes, a and b, and the approach of distant points, δ, read

$$a = \hat{a}\left[\frac{P}{E^*}\right]^{\frac{1}{3}} \tag{2.10}$$

$$b = \hat{b}\left[\frac{P}{E^*}\right]^{\frac{1}{3}} = \frac{a}{A} \tag{2.11}$$

$$\delta = \hat{\delta}\left[\frac{P}{E^*}\right]^{\frac{2}{3}}, \tag{2.12}$$

where $\hat{a}$, $\hat{b}$ and $\hat{\delta}$ are calculated from elliptical integrals and depend only on the relative principal radii of curvature, r_x and r_y; see [33]. The variable E^* denotes an equivalent Young's modulus calculated from the Young's modulus, E_i, and Poisson's ratio, ν_i, $i = 1, 2$, of both bodies

$$\frac{1}{E^*} = \frac{1}{2}\left[\frac{1-\nu_1^2}{E_1} + \frac{1-\nu_2^2}{E_2}\right]. \tag{2.13}$$

The maximum contact pressure,

$$p_0 = \frac{3P}{2\pi ab}\,, \tag{2.14}$$

occurs at the origin, and the pressure distribution in the contact area is ellipsoidal

$$p = p_0\sqrt{1 - \left[\frac{x}{a}\right]^2 - \left[\frac{y}{b}\right]^2}\,. \tag{2.15}$$

To get an impression of the magnitudes of the variables involved, consider the case of a steel wheel and a steel rail both modelled as cylinders with radius $r_{y_1} = 0.3\,\mathrm{m}$

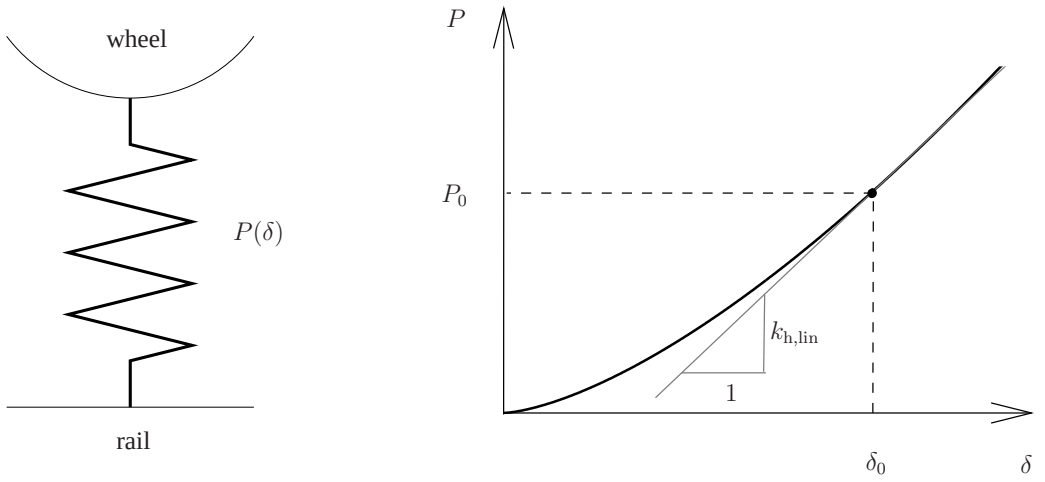

(a) Hertzian spring.

(b) Linearisation of the non-linear spring characteristic.

Figure 2.4: *Implementation of the Hertzian contact model into a wheel/rail interaction model.*

for the rail and $r_{x_2} = 0.46\,\mathrm{m}$ for the wheel. Under a preload $P = 65\,\mathrm{kN}$, the contact ellipse has the semi-axes $a = 6.2\,\mathrm{mm}$ and $b = 4.7\,\mathrm{mm}$, distant points in wheel and rail approach by $\delta = 78\,\mu\mathrm{m}$ and the maximum contact pressure reaches $p_0 = 1.1\,\mathrm{GN/m^2}$.

In many interaction models operating in the time domain, a single non-linear spring is introduced as contact model between wheel and rail (see Figure 2.4(a)). The characteristic, $P(\delta)$, of this spring is obtained from Equation (2.12)

$$P = \left[E^* \hat{\delta}^{\frac{2}{3}}\right] \delta^{\frac{3}{2}} = C_h \, \delta^{\frac{3}{2}} \,. \tag{2.16}$$

The factor C_h is a function only of the principal relative radii of curvature and the material parameters.

Frequently, Equation (2.16) is further simplified. The characteristic is linearised around the approach of distant points, δ_0, corresponding to static preload, P_0, as demonstrated in Figure 2.4(b). The stiffness of the linear Hertzian spring, $k_{\mathrm{h,lin}}$, is obtained from the tangential gradient in the point (δ_0, P_0)

$$k_{\mathrm{h,lin}} = \left.\frac{\mathrm{d}P}{\mathrm{d}\delta}\right|_{\delta_0} = \frac{3}{2} C_h \delta_0^{\frac{1}{2}} = \frac{3}{2}\frac{P_0}{\delta_0} \,. \tag{2.17}$$

In frequency-domain models this linearisation has to be carried out.

2.6 Non-Hertzian models for normal contact

Under the assumptions listed in the previous section, the Hertzian theory gives the exact solution of the normal contact problem. But real wheel and rail surfaces never meet these assumptions exactly and, in consequence, the Hertzian solution can only be an approximate one. In many situations, the Hertzian contact theory might still be sufficient, but it is important to be aware of its limitations. The intention of this section is to discuss the adequacy of the Hertzian contact theory for the wheel/rail contact on the basis of a literature review and to present available non-Hertzian contact models. The focus is hereby on non-Hertzian geometry. The influence of friction and plasticity is not investigated.

Several phenomena lead to deviations from the Hertzian geometry in wheel/rail contact.

The Hertzian contact theory relies on constant radii of curvature of the (undeformed) bodies in the contact area. The radii of curvature of wheel and rail profiles may however change quickly or even jump in lateral direction. Jumps in radius of curvature occur for example for the standard rail profile UIC60, which consists of a sequence of circular arcs with the radii of $300\,\mathrm{mm}$, $80\,\mathrm{mm}$ and $13\,\mathrm{mm}$ [74]. Quick changes in radius of curvature are especially pronounced for worn profiles. As a result of vehicle dynamics, the lateral contact position of the wheel on the rail varies during operation and the changes in radii of curvature in the contact area lead to the formation of non-elliptical contact patches and pressure distributions differing significantly from the Hertzian distribution [28, 70, 74]. Even greater deviations from the Hertzian geometry occur for a wheel flat. In the flat area the radii of curvature of the wheel change quickly and the wheel surface cannot be described by quadratic functions. Baeza et al. [5] compared the impact forces caused by a wheel flat calculated with the Hertzian model and a non-Hertzian model based on influence functions for the elastic half-space and found that the Hertzian model tends to overestimate the peak impact force.

Another important assumption in Hertzian contact theory is that the contacting bodies can be locally approximated by elastic half-spaces for the purpose of contact-stress and deformation calculations. This assumption is valid when the bodies are non-conformal implying that the dimensions of the contact area are small in comparison to the characteristic dimensions of the contacting bodies, e.g. the diameter and the radii of curvature. The half-space assumption is reasonable for wheel/rail tread contact (Figure 2.5(a)), but it is violated for flange contact and contact near the gauge corner of the rail (Figure 2.5(b)) [29]. In the latter case, the flange thickness and the radius of curvature at the gauge corner are of the same order of magnitude as the contact length and the contact is conformal. But this does not necessarily mean that the Hertzian model is a bad choice for all practical cases, where the half-space assumption is obviously not fulfilled. Yan and Fischer [74]

found surprisingly good agreement between the Hertzian pressure distribution and the distribution obtained with a finite-element program for one case of rail gauge corner contact between the rail UIC60 and the wheel UICORE. The work of Wu and Wang [70] indicates, however, that the situation changes when in addition to the violation of the half-space assumption, the radii of curvature of one of the two bodies jump in the contact area. They report errors in maximum contact stress and contact area of up to 72% when comparing the Hertzian solution with the solution obtained with a program for conformal contact.

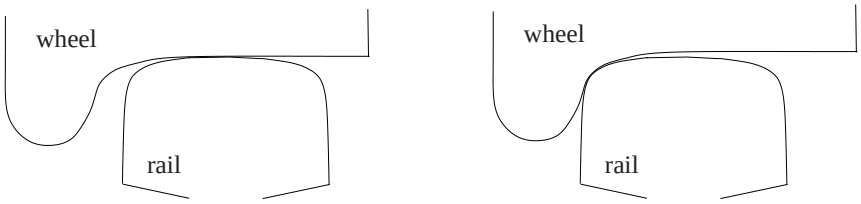

(a) Tread contact. (b) Flange/gauge corner contact.

Figure 2.5: *Wheel/rail contact situations.*

Additionally, the standard Hertzian contact theory is limited to one single contact patch, but the development of two- or multi-point contact is a common phenomenon in wheel/rail interaction. A typical example is the two-point contact for guiding wheels in curves with one contact patch on the wheel tread and one on the wheel flange. Multiple contact patches also occur frequently at other locations on the wheel profile [46].

A fourth phenomenon leading to deviations from the Hertzian geometry is the occurrence of surface roughness. Roughness is not only a source of excitation, but it also changes the geometry of the contacting surfaces and thereby the stiffness of the contact and the size and shape of the contact area. This effect is not included in the Hertzian contact model, which assumes smooth wheel and rail surfaces. In reality, contact does not occur continuously over the whole nominal area of contact, but at many discrete locations, where asperities of the rough surfaces make contact. All the discrete contact locations together form the real area of contact, which is only a fraction of the nominal area of contact. Accordingly, the real contact pressure also differs from the predictions by the Hertzian model. Locally, it is several times higher than the maximum Hertzian pressure [29].

In order to solve the three-dimensional contact problem for arbitrary non-Hertzian geometries, the continuum equations of elasticity have to be solved (see e.g. Appendix A in [26]). This is, in the most general case, only possible numerically, e.g. by using finite-element methods.

If the contacting bodies are subject to certain regularity conditions, the constitutive

relations can be brought into a surface mechanical form [26]:

$$\begin{aligned} \mathbf{u}(\mathbf{x}) &= \int_{\partial V} \mathbf{A}(\mathbf{x},\mathbf{x}^*)\,\mathbf{p}(\mathbf{x}^*)\,\mathrm{d}S \\ u_i(\mathbf{x}) &= \int_{\partial V} \sum_{j=1}^{3} A_{ij}(\mathbf{x},\mathbf{x}^*)\,p_j(\mathbf{x}^*)\,\mathrm{d}S\,, \quad i=1,2,3\,. \end{aligned} \tag{2.18}$$

The displacement $\mathbf{u}$ at a point $\mathbf{x}$ in the body is obtained by integrating over the surface tractions $\mathbf{p}$ on the surface S of the body. The functions $\mathbf{A}(\mathbf{x},\mathbf{x}^*)$, which are called influence functions, indicate the displacement $\mathbf{u}$ at $\mathbf{x}$ due to a point load at surface point $\mathbf{x}^*$. The elastic half-space is one of the few geometries in three-dimensional elasticity for which the influence functions are explicitly known. In the general case they can only be evaluated numerically. This is the reason why the half-space assumption considerably simplifies the solution of the three-dimensional contact problem. The influence functions for the elastic half-space have been derived by Boussinesq [6] and Cerruti [8] and may also be found in [26]. Equations (2.18) with $\mathbf{A}(\mathbf{x},\mathbf{x}^*)$ specified for the elastic half-space are called the Boussinesq-Cerruti integral equations. If the normal elastic displacement, u_3, is assumed not to be influenced by the tangential tractions, p_1 and p_2, the Boussinesq-Cerruti integral equation for the normal displacement, $u_3^{[k]}$, of body k, $k=1,2$, at the surface point $\mathbf{x}=[x_1,x_2,0]^{\mathrm{T}}$ simplifies to

$$u_3^{[k]}(x_1,x_2) = \frac{1-[\nu^{[k]}]^2}{\pi E^{[k]}} \int_{A_c} \frac{p_3(x_1^*,x_2^*)}{\sqrt{[x_1-x_1^*]^2+[x_2-x_2^*]^2}}\,\mathrm{d}x_1^*\mathrm{d}x_2^*\,, \quad k=1,2\,, \tag{2.19}$$

where A_c is the contact area and the normal surface traction, p_3, vanishes outside the contact area. The former assumption implies that the contacting bodies are quasi-identical, which is satisfied e.g. when the two bodies are made of the same material or when both are incompressible. The complete definition of quasi-identity may be found in [26]. As railway wheel and rail are both made of steel, quasi-identity is satisfied in wheel/rail contact.

Many of the contact models published in the 1970s and 1980s for non-Hertzian geometry are a special type of boundary-element approach based on the Boussinesq-Cerruti expressions for the elastic half-space. Only some examples are cited here:

Kalker's programme CONTACT [26, 27], which he developed in the years 1983-1990, is the most successful of these models and is still widely used today. Kalker uses a variational method based on the principle of maximum complementary energy and applies an effective active-set method to solve the contact problem. He discretises the potential contact area with rectangular elements in which the surface traction is constant. Kalker himself calls his method 'exact' [26], which is meant in the sense that the exact Boussinesq-Cerruti equations are implemented [31]. But of

course the method is still subjected to numerical errors and the errors introduced by the half-space assumption. The main advantages and disadvantages of CONTACT are described in the state-of-the-art article about rail (and road) contact mechanics by Knothe et al. [29]. On the one hand, CONTACT is very versatile. It deals with the normal and the tangential problem in rolling contact for arbitrary geometries - as long as the half-space assumption is valid, it handles materials that are not quasi-identical, and provides steady-state and transient solutions. On the other hand, the calculation times are generally considered too high for the implementation into on-line simulations of vehicle system dynamics.

Another contact model was presented by Le-The [31] in 1987. He assumes quasi-identity of the contacting surfaces and starts directly from equation (2.19) to solve the normal contact problem. An additional assumption made by Le-The is that the contacting bodies are bodies of revolution with almost parallel axes, which is approximately true in wheel/rail contact. In this case, the contact area and the normal pressure distribution are almost symmetrical with respect to an axis, y, perpendicular to the rolling direction, x. The contact area can then be discretised in strips in the x-direction that are assigned an elliptical pressure distribution in the rolling direction

$$p_k(x,y) = \hat{p}_k \sqrt{1 - x^2/x_{rk}^2}\,, \tag{2.20}$$

where $\hat{p}_k$ is the maximum pressure amplitude in strip k and x_{rk} is half of the strip length. The pressure in y-direction is assumed constant in each strip. This type of contact elements, which is inspired from line contact and is suitable for slender ellipses [26], had been used before by Reusner [53] and Nayak and Johnson [37], who treated the contact problem for roller bearings. Le-The applied his contact algorithm to the wheel/rail contact problem and showed that the wheel/rail profile combination S1002/UIC60 leads to strongly non-elliptical contact patches, especially at positions where contact-point jumps are encountered for lateral shifting of the rigid wheel profile on the rigid rail profile.

A third contact model was published by Paul and Hashemi in 1981 [45]. They abandoned the half-space assumption and developed a boundary-element approach for conformal contact. Using an approximate analytical expression for the influence function, they solved the conformal contact problem between the railhead and the throat of the wheel flange.

In recent years, two opposing trends are observed in the development of contact algorithms for non-Hertzian geometries. One trend goes to advanced finite-element formulations and another trend goes to approximate and fast solution methods.

The first trend to advanced numerical methods is described by Knothe et al. in their state-of-the-art article from 2001 [29]. Finite-element methods, not being limited to half-spaces, have the capability to include arbitrary contact geometries. In addition, they can account for all kinds of non-linearities such as temperature ef-

fects and plastic deformation. Their drawback is the computational time required. Knothe et al. stated in 2001 [29] that, despite many advances in the field and the development of powerful computers, a solution of the time-dependent problem with a complete three-dimensional contact model was not yet available. Many contributions to the finite-element modelling of the wheel/rail contact have been added in the last few years (see e.g. [10, 55, 57]) but, to my knowledge, Knothe et al.'s statement is still true today.

The second trend to simplified, approximate solutions is outlined in an article by Piotrowski and Chollet [46]. Contact algorithms implemented in online simulations of vehicle system dynamics and high-frequency wheel/rail interaction models have to be fast. Generally, neither the earlier mentioned boundary-element methods nor the finite-element methods meet this requirement. Therefore a lot of effort is made to develop fast, approximate methods that are reliable in non-Hertzian conditions. Piotrowski and Chollet [46] distinguish between two types of methods: (1) multi-Hertzian methods and (2) virtual-penetration methods. The first type of methods has been developed by Pascal and Sauvage [44]. They replace multi-point contacts and non-elliptical contact patches by a set of Hertzian ellipses. They also proposed a method to replace the set of ellipses by a single equivalent ellipse. While the multi-Hertzian method agrees reasonably with Kalker's CONTACT, the equivalent-ellipse method has its limitations. Piotrowski and Chollet [46] estimate that the latter method is still adequate for dynamic simulations, but the former should be used for surface stress analysis and wear calculations. The second type of methods estimates the contact area from the interpenetration area that is obtained by virtually penetrating the undeformed surfaces. Such virtual-penetration methods have been proposed by Ayasse and Chollet [3], Linder [32] and Piotrowski and Kik [47]. Owing to the assumption that the normal stress distribution is elliptical in the direction of rolling in a similar manner as presented in Equation (2.20), these methods are valid for quasi-Hertzian cases, where the contact conditions do not deviate much from Hertzian conditions [46].

A third and widely used type of fast and approximate models for normal contact is based on a bedding of independent springs, the Winkler bedding. These methods are fast because the coupling between different points in the continuum is omitted. Examples of the application of Winkler beddings in wheel/rail contact are the DPRS models proposed by Remington and Webb [48] for the three-dimensional case and by Ford and Thompson [13] for the two-dimensional case. The DPRS models were adapted such that they agree with Hertzian contact for smooth surfaces and then applied to consider roughness with wavelengths down to the millimetre range in the contact area.

To treat the contact problem for surfaces with roughness of even shorter wavelengths down to the micrometre range, two types of models have historically been used: statistical models and deterministic models. The statistical models rely on

a description of the surfaces with some statistical parameters, an assumed simple asperity shape and an assumed asperity height distribution function. The best-known of these models has been proposed by Greenwood and Williamson [18] for nominally flat surfaces and extended by Greenwood and Tripp [17] to the contact of rough spheres. In this model, the surface asperities are approximated by hemispheres that all have the same radius, and a Gaussian distribution of asperity heights is adopted. Alonso and Giménez applied this model with several sets of wheel roughness data and found that the apparent pressure distribution for a typical wheel/rail load condition is almost identical to the Hertzian distribution [1]. The apparent pressure distribution is calculated by dividing the force calculated in a small surface element by the area of the element. Deterministic models solve the contact problem for the actual measured surface topography. Such a model has recently been applied by Bucher et al. to the wheel/rail contact [7]. They pointed out that the results are dependent on the wavelength content of the measured roughness, which is influenced by the measurement resolution and the data processing. The shorter the wavelengths considered, the more the real area of contact decreases and the more the real pressure distribution becomes cleft. The results of Bucher et al. are partly contradictory to results obtained with the simpler Greenwood/Tripp model. It still seems to be an open question whether and in which way micro-roughness influences the wheel/rail interaction.

Independently of this question, it is unrealistic to include contact models with a resolution in the micrometre range into wheel/rail interaction models, due to the high computational effort and the lack of input data. As already mentioned, however, it is possible to include the roughness distribution with a lower resolution and thereby consider the effect of roughness wavelengths in the order of the contact dimensions.

The literature review showed that significant errors may occur if Hertzian contact theory is used in cases where the radii of curvature are not constant in the contact area. It is as yet difficult to draw a general final conclusion about the applicability of Hertzian contact in wheel/rail contact. The problem is that in all investigations only some specific examples and/or simplified geometries have been considered. An extensive investigation of contact between different real wheel and rail surfaces would be needed in order to decide whether the errors occurring when using Hertzian contact theory for non-Hertzian geometry are still acceptable in praxis. The answer to this question certainly depends also on the purpose of investigation. In cases where only the total normal force is of interest, Hertzian contact theory has a wider range of applicability than in e.g. wear calculations where the pressure distribution and size and shape of the contact area are of interest.

Chapter 3

Implementation of a wheel/rail interaction model in the time domain

Based on the literature review presented in the previous chapter, the requirements on the vertical wheel/rail interaction model developed in this thesis can now be specified and modelling choices can be motivated.

In order to include the non-linearities occurring in the contact zone, the interaction model has to be formulated in the time domain. Non-linearities cannot be neglected in the case of discrete irregularities, and are also important in the case of severe roughness and/or low static preload. As calculation times for time-domain models are generally high, special attention has to be given to computational efficiency. An efficient technique that has been pointed out in the literature review is the representation of track and wheel by Green's functions, which can be pre-calculated before starting the dynamic simulations. This technique will be used here. On the one hand, the usage of Green's functions implies a simplification since only linear wheel and track models can be represented by Green's functions. On the other hand, this approach is very versatile because any wheel or rail model represented by a Green's function can be used without changing the mathematical formulation of the interaction model.

The wheel and track model should represent with sufficient precision the dynamic behaviour of wheel and track in the frequency range of interest, which has been identified as the range from $100\,\mathrm{Hz}$ to $5\,\mathrm{kHz}$. As it is generally considered sufficient to include the wheel as a rigid mass for vertical interaction, the wheel model is kept simple. The track model comprises a Rayleigh-Timoshenko beam model of the rail and discrete supports. The cross-sectional deformations occurring at high frequencies are thus not included and according to the discussion in *Section 2.4* the validity of the track model above about $2.5\,\mathrm{kHz}$ has to be questioned. This is however not seen as critical, since a track model including cross-sectional deformation, if it were available, could be included in the interaction model in exactly the same manner as the presently applied model. Wheel and track model and their respective representation as Green's functions are presented in detail in *Section 3.1* and *3.2*.

The question whether the Hertzian contact model is sufficient for vertical wheel/rail

interaction could not be answered completely in the literature review. For this reason, two non-Hertzian contact models are developed in this thesis, which allow contributing to the clarification of this question. A two-dimensional model is presented in *Section 3.3* and a three-dimensional one in *Section 3.4*. These two models include the contact-filter effect dynamically and do not require the calculation of an equivalent roughness as pre-processing step.

3.1 Wheel model

The vehicle model includes (half) the wheelset mass and the primary suspension. All the vehicle components above the primary suspension of the wheel are simplified to a static preload, P.

Two different wheel models of this type are introduced. The first wheel model, model A, is a one-degree-of-freedom system comprising (half) the wheelset mass, M_{W}, and the primary suspension consisting of a spring with constant k_{S} in parallel with a damper with constant c_{S} (see Figure 3.1). The vertical position of the centre

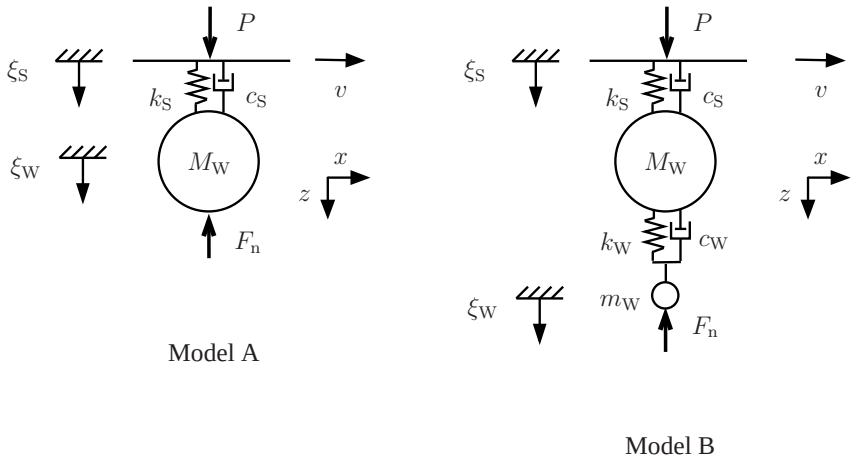

Figure 3.1: Wheel modelled as single-degree-of-freedom system (model A) and two-degree-of-freedom system (model B).

of gravity of the wheel centre is described by the coordinate ξ_{W}, and the position of the suspension by ξ_{S}. Clamping the suspension, the wheel is represented in the frequency domain by its receptance, $\tilde{G}_{\mathrm{W}}(f)$,

$$\tilde{G}_{\mathrm{W}}(f) = \frac{\xi_{\mathrm{W}}(f)}{F_{\mathrm{n}}(f)} \tag{3.1}$$

which indicates the displacement response, $\xi_{\mathrm{W}}(f)$, to a harmonically exciting contact force, $F_{\mathrm{n}}(f)$, at frequency f (see Figure 3.2).

The second wheel model, model B, is a two-degree-of-freedom system that includes in comparison to model A an additional small mass, m_{W}, and an additional spring with constant k_{W} in parallel with a damper with constant c_{W} (see Figure 3.1). These additional components do not have a direct physical meaning, but can be used to tune the receptance in the higher frequency range to resemble the receptance obtained with a finite-element model [40]. This type of wheel model has shown good performance in previous studies by Nielsen [40] and Wu and Thompson [72].

Figure 3.2 shows a comparison of the receptance of the two wheel models for the numerical values of the parameters $M_{\mathrm{W}} = 592.5\,\mathrm{kg}$, m_{W}=3 kg, $k_{\mathrm{S}} = 1.12\,\mathrm{MN/m}$, $c_{\mathrm{S}} = 13.2\,\mathrm{kNs/m}$, $k_{\mathrm{W}} = 2.4\,\mathrm{GN/m}$ and $c_{\mathrm{W}} = 155\,\mathrm{kNs/m}$. For this configuration, the receptances differ from each other from above about $100\,\mathrm{Hz}$.

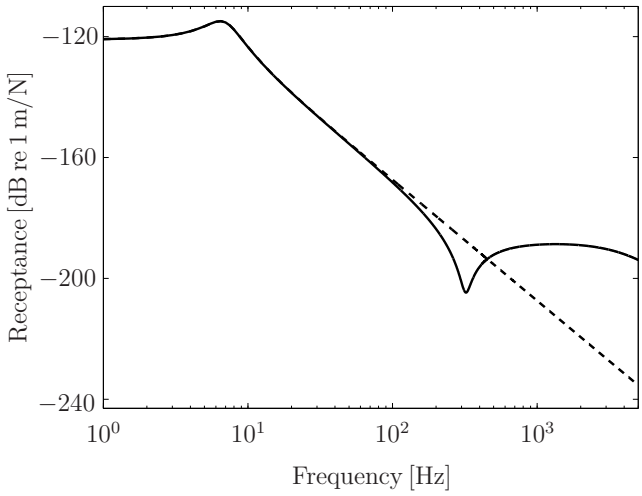

Figure 3.2: Magnitude of the wheel receptance: Model A (− − −), Model B (———).

In the time domain, the wheel is represented by its impulse response function (Green's function), $\tilde{g}_{\mathrm{W}}(t)$, which is obtained from the receptance by an inverse Fourier transform:

$$\tilde{g}_{\mathrm{W}}(t) = \mathscr{F}^{-1}\left(\tilde{G}_{\mathrm{W}}(f)\right) . \tag{3.2}$$

The Green's functions of both wheel models appear almost identical as can be seen in Figure 3.3. It should however be noted that the scale in Figure 3.3 is linear and therefore does not allow identifying differences in the dynamics at lower levels.

In the interaction model, the static preload, P, is applied by pressing the wheel onto the rail until the static contact force equals P. The suspension is fixed in the corresponding position

$$\xi_{\mathrm{S}} = \xi_{\mathrm{S}}(P) . \tag{3.3}$$

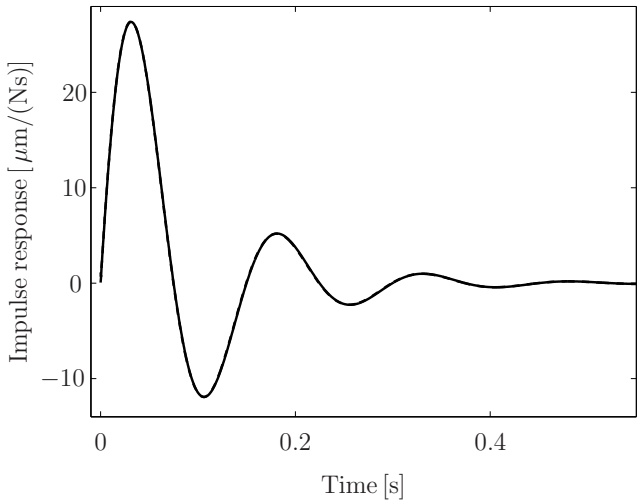

Figure 3.3: Impulse response of the wheel: Model A (– – –), Model B (———). The curves are almost identical.

In the dynamic calculations, the wheel is then moved over the rail in the x-direction with constant velocity v. The position of the wheel centre on the rail at time t is indicated by the coordinate $x = v\,t$. In order to describe the variables in the contact zone, an additional moving coordinate axis x' with the origin at x is introduced. It is assumed that the contact pressure distribution $p(x, x')$ which excites the wheel to vibrate in the z-direction can be represented by the total normal contact force, F_{n}, with the point of attack vertically below the wheel centre at x, which is called the nominal contact point (see Figure 3.4).

The normal displacement of the wheel centre, $\xi_{\mathrm{W}}(t)$, is obtained by convoluting

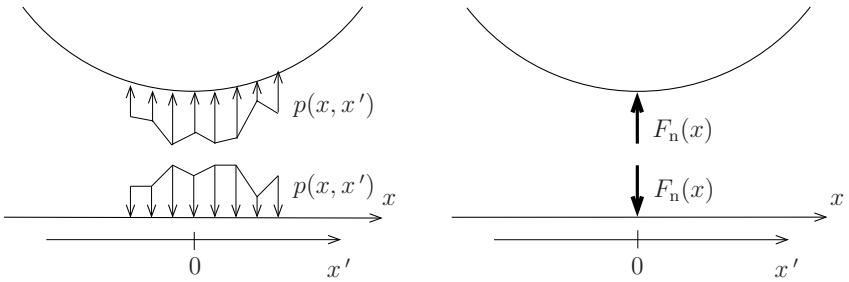

Figure 3.4: Simplification of the excitation: Wheel and rail are assumed to be excited by the point force F_{n} (right-hand side) instead of the pressure distribution p (left-hand side).

the normal contact force with the Green's function of the wheel

$$\xi_{\mathrm{W}}(t) = -\int_0^t F_{\mathrm{n}}(\tau)\tilde{g}_{\mathrm{W}}(t-\tau)\,\mathrm{d}\tau + \xi_{\mathrm{S}}(P)\,. \tag{3.4}$$

Introducing the time increment Δt and the discrete time vector with the elements

$$t(\alpha) = [\alpha - 1]\Delta t, \quad \alpha = 1, 2, \ldots N_t\,, \tag{3.5}$$

the discretised version of Equation (3.4) at time step α reads

$$\xi_{\mathrm{W}}(\alpha) = -\sum_{n=1}^{N_{\mathrm{W}}} g_{\mathrm{W}}(n)\, F_{\mathrm{n}}(\alpha - n + 1) + \xi_{\mathrm{S}}(P)\,, \tag{3.6}$$

where $g_{\mathrm{W}}(n)$ is the discrete version of the Green's function of the wheel having N_{W} elements

$$\begin{aligned} g_{\mathrm{W}}(1) &= \frac{1}{2}\,\Delta t\,\tilde{g}_{\mathrm{W}}(0) \\ g_{\mathrm{W}}(n) &= \Delta t\,\tilde{g}_{\mathrm{W}}(n-1) \quad \text{for } n = 2, 3 \ldots N_{\mathrm{W}} - 1 \\ g_{\mathrm{W}}(N_{\mathrm{W}}) &= \frac{1}{2}\,\Delta t\,\tilde{g}_{\mathrm{W}}\left([N_{\mathrm{W}} - 1]\Delta t\right)\,. \end{aligned} \tag{3.7}$$

At $N_{\mathrm{W}}\,\Delta t$, the Green's function is assumed to have decayed to zero.

At time step α, the forces at previous time steps are known and the only unknown force is $F_{\mathrm{n}}(\alpha)$. The sum in Equation (3.6) can therefore be split up into an unknown term containing $F_{\mathrm{n}}(\alpha)$ and a known term denoted $\xi_{\mathrm{W}}^{\mathrm{old}}(\alpha)$

$$\begin{aligned} \xi_{\mathrm{W}}(\alpha) &= -g_{\mathrm{W}}(1)F_{\mathrm{n}}(\alpha) - \sum_{n=2}^{N_{\mathrm{W}}} g_{\mathrm{W}}(n)\, F_{\mathrm{n}}(\alpha - n + 1) + \xi_{\mathrm{S}}(P) \\ &= -g_{\mathrm{W}}(1)F_{\mathrm{n}}(\alpha) - \xi_{\mathrm{W}}^{\mathrm{old}}(\alpha) + \xi_{\mathrm{S}}(P)\,. \end{aligned} \tag{3.8}$$

3.2 Track model

The track model is a linear finite-element model based on a rail description by Rayleigh-Timoshenko beam elements. This model is implemented in the wheel/rail interaction model DIFF [41] and could be used by courtesy of Jens Nielsen.

The track model takes into account discrete supports and has a length of 70 sleeper bays with sleeper spacing L_{S}. Both rail ends are clamped. The rail, which is a UIC60 rail with bending stiffness EI, shear stiffness kGA and mass per unit beam length m', is modelled by eight Rayleigh-Timoshenko beam elements per sleeper bay. The discrete supports are composed of railpads and sleepers on ballast; see

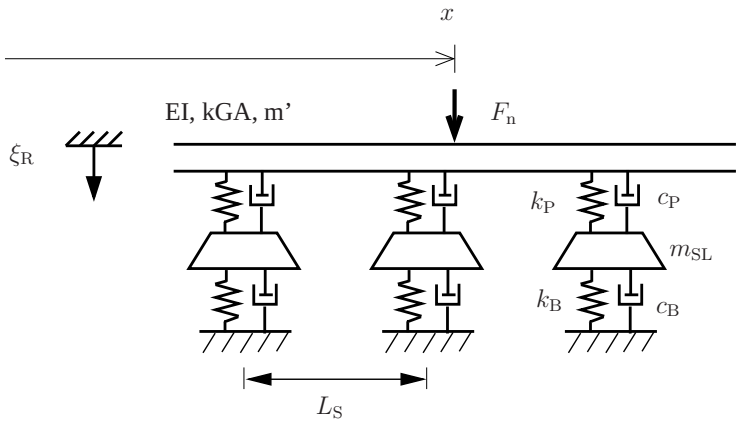

Figure 3.5: Rail model with discrete supports.

Figure 3.5. The railpads are represented by a spring with stiffness k_P in parallel with a viscous damper with constant c_P. The sleepers are modelled as rigid masses m_SL and the ballast is represented by a spring with stiffness k_B in parallel with a viscous damper with constant c_B.
Figure 3.6 shows the magnitude of the track point receptance, $\tilde{G}_\mathrm{R}^{x_0,\,x_0}$, for two different excitation positions x_0. The numerical values of the parameters used are $EI = 6.4\,\mathrm{MNm^2}$, $kGA = 250\,\mathrm{MN}$, $m' = 60\,\mathrm{kg/m}$, $L_\mathrm{S} = 0.65\,\mathrm{m}$, $k_\mathrm{P} = 120\,\mathrm{MN/m}$, $c_\mathrm{P} = 16\,\mathrm{kNs/m}$, $m_\mathrm{SL} = 125\,\mathrm{kg}$, $k_\mathrm{B} = 140\,\mathrm{MN/m}$ and $c_\mathrm{B} = 165\,\mathrm{kNs/m}$. For excitation at midspan between two sleeper positions, $x_0 = 0.5\,L_\mathrm{S}$, a sharp peak is observed at $943\,\mathrm{Hz}$, which is the pinned-pinned resonance frequency. Correspondingly, the point receptance for excitation over a sleeper, $x_0 = 0$, shows an anti-resonance in this frequency range, which has slightly shifted to higher frequencies. Additionally, the receptances for both excitation positions have an anti-resonance at about $2640\,\mathrm{Hz}$. A detailed description of the track model is given in references [41] and [39].

In the wheel/rail interaction model, the discretely supported rail is represented by moving Green's functions, $\tilde{g}_{\mathrm{R},v}^{x_0}(t)$ [43]. For excitation of the rail (index R) at the position x_0 at time $t_0 = 0$, the function $\tilde{g}_{\mathrm{R},v}^{x_0}(t)$ describes the displacement response of the rail at a point moving at train speed v away from the excitation, thus at the nominal contact point between wheel and rail.

In the interaction model, the normal displacement of the rail, $\xi_\mathrm{R}(t)$, is calculated by convoluting the contact force with the moving Green's functions of the rail

$$\xi_\mathrm{R}(t) = \int_0^t F_\mathrm{n}(\tau)\tilde{g}_{\mathrm{R},v}^{v\tau}(t-\tau)\,\mathrm{d}\tau\,. \tag{3.9}$$

The discrete version of $\tilde{g}_{\mathrm{R},v}^{x_0}(t)$, denoted $g_{\mathrm{R},v}^{x_0}(n)$, is constructed from a series of track receptances, $\tilde{G}_\mathrm{R}^{x_0,\,x_0+\chi}(f)$. The superscripts specify the excitation point, x_0,

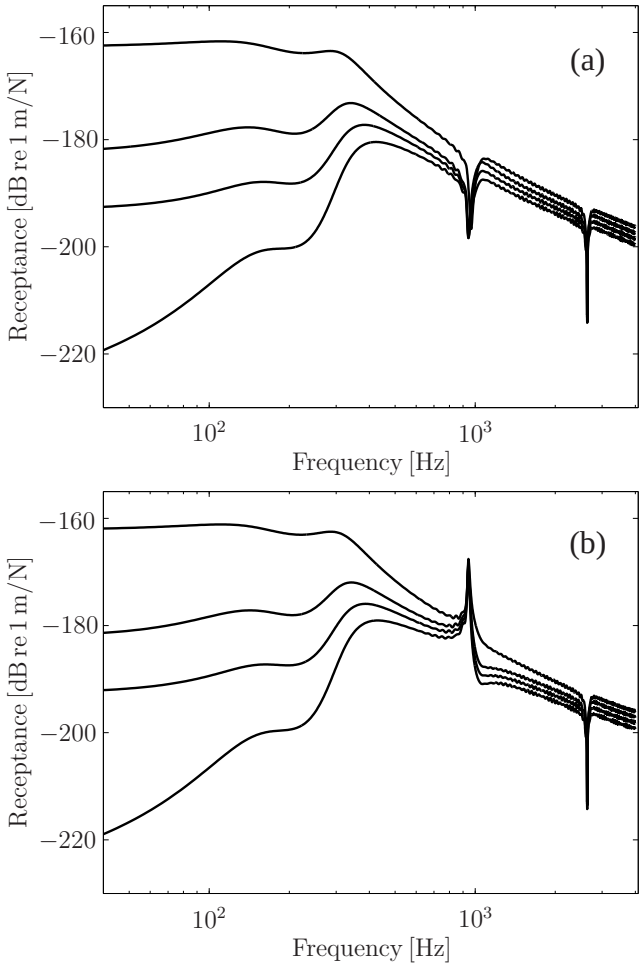

Figure 3.6: Magnitude of the track point- and cross-receptances for excitation (a) above a sleeper position, $x_0 = 0$, and (b) at midspan between two sleeper positions, $x_0 = 0.5\,L_\mathrm{S}$: the plotted curves are from upper to lower $|\tilde{G}_\mathrm{R}^{x_0,\,x_0}|$, $|\tilde{G}_\mathrm{R}^{x_0,\,x_0+2\,L_\mathrm{S}}|$, $|\tilde{G}_\mathrm{R}^{x_0,\,x_0+4\,L_\mathrm{S}}|$ and $|\tilde{G}_\mathrm{R}^{x_0,\,x_0+6\,L_\mathrm{S}}|$.

and the response point, $x_0 + \chi$. Eight examples of these receptances are shown in Figure 3.6. The Green's functions, $\tilde{g}_{\mathrm{R}}^{x_0,\, x_0+\chi}(t)$, corresponding to the track receptances, are obtained by inverse Fourier transform

$$\tilde{g}_{\mathrm{R}}^{x_0,\, x_0+\chi}(t) = \mathscr{F}^{-1}\left(\tilde{G}_{\mathrm{R}}^{x_0,\, x_0+\chi}(f)\right) . \tag{3.10}$$

Exploiting the coupling

$$\Delta x = v\Delta t \tag{3.11}$$

between the time increment, Δt, and the space increment, Δx, the discrete moving Green's functions are constructed as

$$\begin{aligned} g_{\mathrm{R},v}^{x_0}(1) &= \frac{1}{2}\Delta t\, \tilde{g}_{\mathrm{R}}^{x_0,\, x_0}(0) \\ g_{\mathrm{R},v}^{x_0}(n) &= \Delta t\, \tilde{g}_{\mathrm{R}}^{x_0,\, x_0+[n-1]\Delta x}([n-1]\Delta t) \quad \text{for } n = 2, 3 \ldots N_{\mathrm{R}} - 1 \\ g_{\mathrm{R},v}^{x_0}(N_{\mathrm{R}}) &= \frac{1}{2}\Delta t\, \tilde{g}_{\mathrm{R}}^{x_0,\, x_0+[N_{\mathrm{R}}-1]\Delta x}([N_{\mathrm{R}}-1]\Delta t) \end{aligned} \tag{3.12}$$

where N_{R} is the number of samples. At $N_{\mathrm{R}}\Delta t$, the Green's functions of the rail are assumed to have decayed to zero. Examples of moving Green's functions for two different excitation positions and three different velocities are presented in Figure 3.7. The additional high-frequency oscillations for excitation at $x_0 = 0.5\, L_{\mathrm{S}}$ (Figure 3.7(b)) in comparison to excitation at $x_0 = 0$ (Figure 3.7(a)) are explained by the pinned-pinned resonance. Due to the periodicity of the track, $L_{\mathrm{S}}/\Delta x$ different moving Green's functions suffice to represent the track at each velocity v. With the parameters $L_{\mathrm{S}} = 0.65\,\mathrm{m}$ and $\Delta x = 1\,\mathrm{mm}$, this leads to 650 moving Green's functions.

The discrete version of Equation (3.9) formulated at time step α reads

$$\xi_{\mathrm{R}}(\alpha) = \sum_{n=1}^{N_{\mathrm{R}}} g_{\mathrm{R},v}^{v[\alpha-n]\Delta t}(n)\, F_{\mathrm{n}}(\alpha - n + 1) . \tag{3.13}$$

Analogous to Equation (3.8), this equation can be split up into a part containing the only unknown force, $F_{\mathrm{n}}(\alpha)$, and the known part, $\xi_{\mathrm{R}}^{\mathrm{old}}(\alpha)$,

$$\begin{aligned} \xi_{\mathrm{R}}(\alpha) &= g_{\mathrm{R},v}^{v[\alpha-1]\Delta t}(1) F_{\mathrm{n}}(\alpha) + \sum_{n=2}^{N_{\mathrm{W}}} g_{\mathrm{R},v}^{v[\alpha-n]\Delta t}(n)\, F_{\mathrm{n}}(\alpha - n + 1) \\ &= g_{\mathrm{R},v}^{v[\alpha-1]\Delta t}(1) F_{\mathrm{n}}(\alpha) + \xi_{\mathrm{R}}^{\mathrm{old}}(\alpha) . \end{aligned} \tag{3.14}$$

3.3 Contact model A: Winkler bedding

The first of the two non-linear and non-Hertzian contact models presented in this chapter is a two-dimensional model. It is based on a Winkler bedding consisting

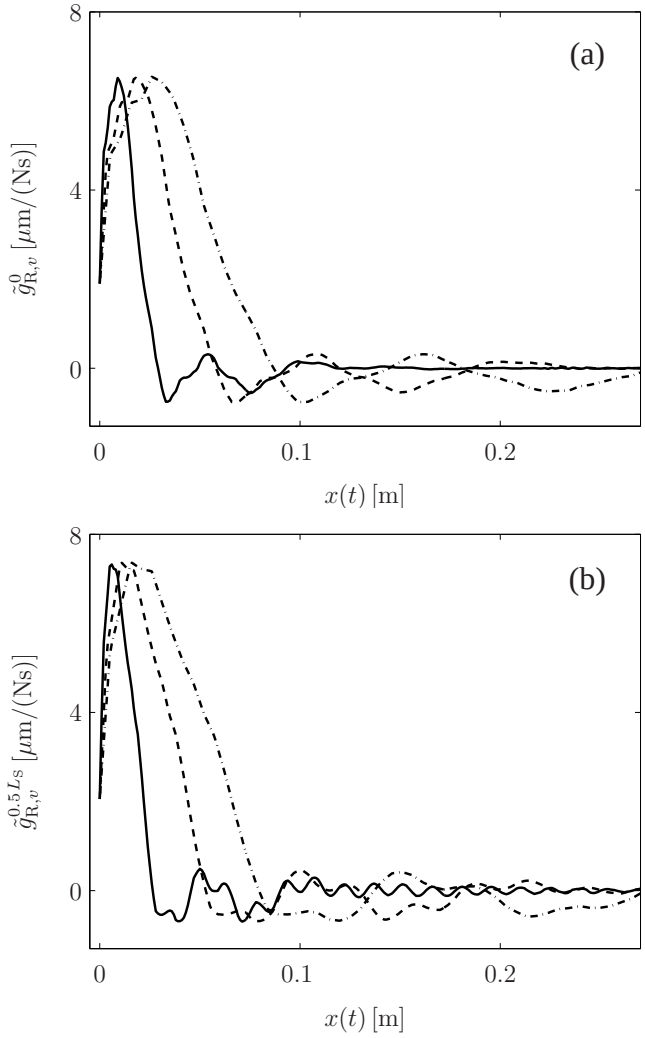

Figure 3.7: Moving Green's functions of the track for excitation (a) above a sleeper position, $x_0 = 0$, and (b) at midspan between two sleeper positions, $x_0 = 0.5\,L_\mathrm{S}$: —— $v = 50\,\mathrm{km/h}$, $- - -$ $v = 100\,\mathrm{km/h}$, $-\cdot-$ $v = 150\,\mathrm{km/h}$.

of independent springs introduced between wheel and rail (see Figure 3.8). The model considers the roughness profile in one longitudinal line throughout the contact patch. For simplicity, only the rail is displayed as rough in Figure 3.8, but both

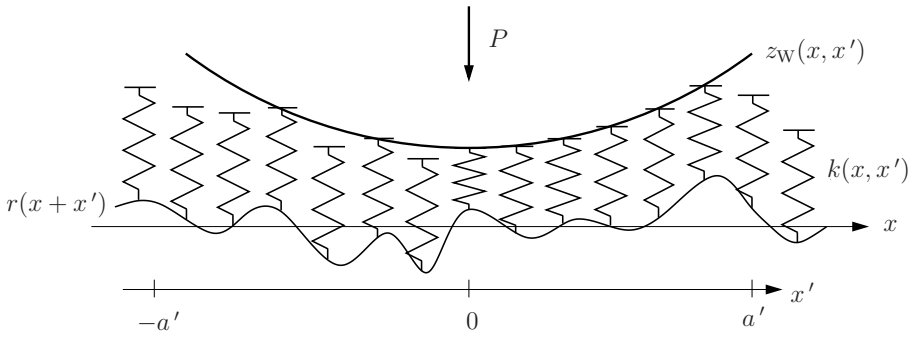

Figure 3.8: Bedding model for the wheel/rail contact.

wheel and rail are considered as rough. The combined roughness is contained in the variable $r(x)$, which is defined as positive for an asperity on the rail.

For the wheel positioned at x, the deflection, $\Delta\zeta(x, x')$, of all involved contact springs depends on the wheel displacement, $\xi_{\mathrm{W}}(x)$, the rail displacement, $\xi_{\mathrm{R}}(x)$, the combined roughness, $r(x + x')$, and the wheel profile, $z_{\mathrm{W}}(x, x')$, as

$$\Delta\zeta(x, x') = \xi_{\mathrm{W}}(x) - \xi_{\mathrm{R}}(x) + r(x + x') - z_{\mathrm{W}}(x, x')\,. \tag{3.15}$$

The total contact force is obtained by an integration over the bedding

$$F_{\mathrm{n}}(x) = \int_{-a'}^{a'} \tilde{k}(x, x')\,\Delta\zeta(x, x')\,\mathrm{d}x\,, \tag{3.16}$$

which has a stiffness per unit length

$$\tilde{k}(x, x') = \begin{cases} \frac{1}{2}\frac{E}{[1-\nu^2]} & \text{for} \quad \Delta\zeta(x, x') \geq 0 \\ 0 & \text{for} \quad \Delta\zeta(x, x') < 0 \end{cases}\,, \tag{3.17}$$

where E is the Young's modulus and ν the Poisson's ratio of rail and wheel (assumed to be of the same material). The integration domain, $[-a', a']$, has to be chosen as long enough to include all potential points of contact. Loss of contact can occur for each of the springs in the bedding. This takes place if $\Delta\zeta(x, x') < 0$. In this case, the stiffness, $\tilde{k}(x, x')$, is set to zero.

The choice of $\tilde{k}(x, x')$ in Equation (3.17) makes it possible for the bedding to correctly model the contact length, total contact load and deflection as predicted by the Hertzian theory for smooth surfaces if, in addition, the wheel radius is adjusted according to [13]

$$R_{\mathrm{W}}^{\mathrm{m}} = \frac{1}{2}R\,. \tag{3.18}$$

The radius R is the original radius of curvature of the conical wheel in the rolling direction, which is assumed to equal the transverse radius of curvature of the straight rail.

Introducing $2N_{\mathrm{C}}+1$ contact springs at the discrete positions

$$x'(\beta) = \beta\,\Delta x, \quad \beta = -N_{\mathrm{C}}, -N_{\mathrm{C}}+1, -N_{\mathrm{C}}+2, \ldots, N_{\mathrm{C}}\,, \tag{3.19}$$

the discrete versions of Equations (3.15)-(3.17) formulated at time step α corresponding to time $(\alpha-1)\Delta t$ and wheel centre position on the rail $(\alpha-1)\Delta x$ read

$$\Delta\zeta(\alpha,\beta) = \xi_{\mathrm{W}}(\alpha) - \xi_{\mathrm{R}}(\alpha) + r(\alpha+\beta) - z_{\mathrm{W}}(\alpha,\beta) \tag{3.20}$$

$$F_{\mathrm{n}}(\alpha) = \sum_{\beta=-N_{\mathrm{C}}}^{N_{\mathrm{C}}} k(\alpha,\beta)\,\Delta\zeta(\alpha,\beta) \tag{3.21}$$

$$k(\alpha,\beta) = \begin{cases} \frac{1}{2}\frac{E}{[1-\nu^2]}\Delta x & \text{for} \quad \Delta\zeta(\alpha,\beta) \geq 0 \\ 0 & \text{for} \quad \Delta\zeta(\alpha,\beta) < 0 \end{cases} \tag{3.22}$$

Equations (3.20)-(3.22) together with Equations (3.8) and (3.14) form a non-linear equation system that can be solved for $F_{\mathrm{n}}(\alpha)$ by applying the Newton-Raphson method. The desired $F_{\mathrm{n}}(\alpha)$ is the root of the function

$$f(F_{\mathrm{n}}(\alpha)) = F_{\mathrm{n}}(\alpha) - \sum_{\beta=-N_{\mathrm{C}}}^{N_{\mathrm{C}}} k(\alpha,\beta)\,\Delta\zeta(\alpha,\beta)\,, \tag{3.23}$$

which can be seen from Equation (3.21). This root is obtained by iteration

$$F_{\mathrm{n}}^{[\gamma+1]}(\alpha) = F_{\mathrm{n}}^{[\gamma]}(\alpha) - \frac{f(F_{\mathrm{n}}^{[\gamma]}(\alpha))}{f'(F_{\mathrm{n}}^{[\gamma]}(\alpha))}\,, \tag{3.24}$$

where

$$\begin{aligned} & f'\left(F_{\mathrm{n}}(\alpha)\right) \\ &= \frac{\mathrm{d}\,f\left(F_{\mathrm{n}}(\alpha)\right)}{\mathrm{d}\,F_{\mathrm{n}}(\alpha)} \\ &= 1 - \sum_{\beta=-N_{\mathrm{C}}}^{N_{\mathrm{C}}} \left\{ \frac{\mathrm{d}\,k(\alpha,\beta)}{\mathrm{d}\,F_{\mathrm{n}}(\alpha)}\,\Delta\zeta(\alpha,\beta) + k(\alpha,\beta)\frac{\mathrm{d}\,\Delta\zeta(\alpha,\beta)}{\mathrm{d}\,F_{\mathrm{n}}(\alpha)} \right\} \\ &= 1 - \sum_{\beta=-N_{\mathrm{C}}}^{N_{\mathrm{C}}} \left\{ k(\alpha,\beta)\frac{\mathrm{d}\,\Delta\zeta(\alpha,\beta)}{\mathrm{d}\,F_{\mathrm{n}}(\alpha)} \right\} \end{aligned} \tag{3.25}$$

Inserting Equations (3.20), (3.8) and (3.14) the derivative reads

$$f'\left(F_{\mathrm{n}}(\alpha)\right) = 1 + \left[g_{\mathrm{W}}(1) + g_{\mathrm{R,v}}^{v[\alpha-1]\Delta t}(1)\right] \sum_{\beta=-N_{\mathrm{C}}}^{N_{\mathrm{C}}} k(\alpha,\beta)\,. \tag{3.26}$$

After determining $F_{\mathrm{n}}(\alpha)$, the unknown displacements $\xi_{\mathrm{W}}(\alpha)$ and $\xi_{\mathrm{R}}(\alpha)$ are obtained by applying Equations (3.8) and (3.14).

3.4 Contact model B: Elastic half-space model

The contact model based on the Winkler bedding presented in the previous section is computationally efficient and allows considering the contact-filter effect in a natural way. Yet the model is only a two-dimensional one, and only the roughness in one line in the longitudinal x-direction is taken into account. Additionally, the springs in the bedding deform independently of each other, while the points in a real continuum are coupled to each other. This requires reducing the wheel radius in order to simulate Hertz contact for smooth surfaces.

An alternative contact model that overcomes these shortcomings is based on the influence functions for the elastic half-space. If one assumes that wheel and rail are quasi-identical and can be locally approximated by elastic half-spaces, the relation between the normal displacement of one of the two surfaces and the surface pressure distribution is expressed by Equation (2.19), which is repeated here

$$u^{[k]}(x',y') = \frac{1-[\nu^{[k]}]^2}{\pi E^{[k]}} \int_{A_c} \frac{p(x^*,y^*)}{\sqrt{[x'-x^*]^2+[y'-y^*]^2}}\,\mathrm{d}x^*\mathrm{d}y^*\,, \quad k=1,2\,. \tag{3.27}$$

For simplicity of the notation, p_3 and u_3 are now denoted p and u. Evaluating this

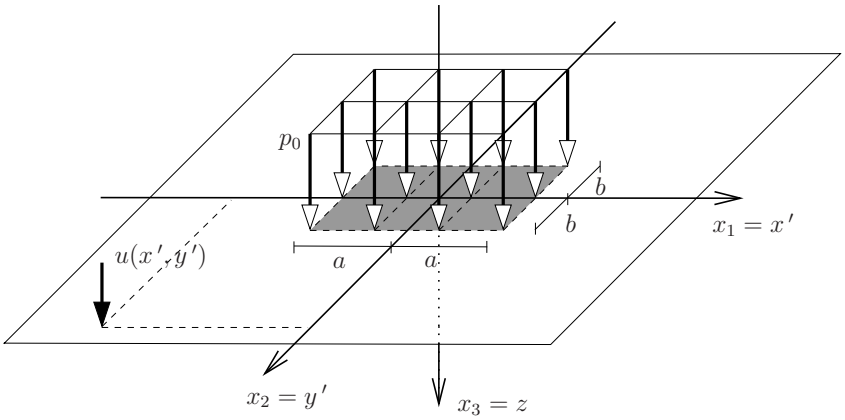

Figure 3.9: Elastic half-space loaded in a rectangular area $2a \times 2b$.

integral for a pressure distribution $p(x^*, y^*) = p_0$ that is constant in a rectangular area $2a \times 2b$ located at the origin (Figure 3.9) and zero outside, an analytical expression is obtained [25]

$$\begin{aligned}
\frac{\pi E^{[k]}}{1-[\nu^{[k]}]^2}\,\frac{u^{[k]}(x',y')}{p_0} &= [x'+a]\,\ln\left(\frac{[y'+b]+\{[y'+b]^2+[x'+a]^2\}^2}{[y'-b]+\{[y'-b]^2+[x'+a]^2\}^2}\right)\\
&+ [y'+b]\,\ln\left(\frac{[x'+a]+\{[y'+b]^2+[x'+a]^2\}^2}{[x'-a]+\{[y'+b]^2+[x'-a]^2\}^2}\right)\\
&+ [x'-a]\,\ln\left(\frac{[y'-b]+\{[y'-b]^2+[x'-a]^2\}^2}{[y'+b]+\{[y'+b]^2+[x'-a]^2\}^2}\right)\\
&+ [y'-b]\,\ln\left(\frac{[x'-a]+\{[y'-b]^2+[x'-a]^2\}^2}{[x'+a]+\{[y'-b]^2+[x'+a]^2\}^2}\right)\\
&= C(x',y',a,b) \qquad\qquad k=1,2\,. \qquad (3.28)
\end{aligned}$$

Both the rail (body 1) and the wheel (body 2) are approximated by elastic half-spaces with the z_k-axes pointing into the bodies. The combined displacement, u, due to the uniform pressure distribution, p_0, from Figure 3.9 is then

$$\begin{aligned}
u(x',y') &= u^{[1]}(x',y') + u^{[2]}(x',y')\\
&= \left[\frac{1-{\nu^{[1]}}^2}{E^{[1]}} + \frac{1-{\nu^{[2]}}^2}{E^{[2]}}\right]\frac{p_0}{\pi}\,C(x',y',a,b)\,. \qquad (3.29)
\end{aligned}$$

As wheel and rail are generally both made of steel, the elastic constants are identical, $E^{[1]} = E^{[2]} = E$ and $\nu^{[1]} = \nu^{[2]} = \nu$, and one obtains

$$u(x',y') = 2\,\frac{1-\nu^2}{\pi E}\,p_0\,C(x',y',a,b)\,. \qquad (3.30)$$

A surface region of the elastic half-spaces is now assumed to be discretised into a grid of N_e rectangular elements with their centres located at $({x_i}', {y_i}')$. If each of the elements is loaded with a uniform pressure distribution, the resulting combined displacement field, $\mathbf{u}$, can be calculated by applying Equation (3.30) for all combinations of source and receiver elements and superposing the results. For this purpose, the coordinates (x', y') on the right-hand side of Equation (3.30) have to be replaced by $(x'-\bar{x}, y'-\bar{y})$, where $(\bar{x}, \bar{y})$ indicates the position of the centre of the momentarily considered source element and (x', y') the position of the centre of the momentarily considered receiver element. This procedure can be summarised in a matrix equation of the type

$$\mathbf{u} = \mathbf{C}\,\mathbf{p} \qquad (3.31)$$

$$u_i = \sum_{j=1}^{N_\mathrm{e}} C_{ij} p_j\,, \quad i = 1,2,3\ldots N_\mathrm{e}\,, \qquad (3.32)$$

where the coefficients C_{ij} are calculated from

$$C_{ij} = C(x'_i - \bar{x}_j, y'_i - \bar{y}_j, a, b)\,. \tag{3.33}$$

The matrix $\mathbf{C}$ of size $N_\mathrm{e} \times N_\mathrm{e}$ is called the influence matrix and vector $\mathbf{p}$ of length N_e contains the pressure amplitudes for all elements. The vector $\mathbf{u}$ of length N_e contains the combined displacement for all element centres. If the rectangular elements are chosen sufficiently small, Equation (3.31) can be used to approximate the relation between an arbitrary pressure distribution on the elastic half-spaces and the resulting displacement field.

The total contact force, F_n, is obtained by integrating the pressure distribution

$$F_\mathrm{n}(x) = \int_A p(x, x', y')\,\mathrm{d}x'\mathrm{d}y'\,, \tag{3.34}$$

where A is the integration area containing the contact area. The discretised version of this equation reads

$$F_\mathrm{n}(\alpha) = \sum_{i=1}^{N_\mathrm{e}} p_i(\alpha)\,A_i\,, \tag{3.35}$$

where A_i is the area belonging to element i.

Equations (3.31) and (3.35) can be applied to solve the three-dimensional normal contact problem of the moving wheel on the rail, if the origin of the x'- and y'-axes is displaced with the position, x, of the nominal contact point. Additionally, a kinematic constraint equation such as Equation (3.15) has to be introduced. As the points of the elastic half-space are coupled in contrast to the springs in the Winkler bedding, the kinematic constraint equation (3.15) has to be extended. The spring deflection, $\Delta\zeta$, is replaced by the combined surface displacement, $\boldsymbol{u}$, and the distance, $\mathbf{d}$, between the deformed bodies is introduced:

$$\mathbf{d}(x) = \boldsymbol{\xi}_\mathbf{R}(x) - \boldsymbol{\xi}_\mathbf{W}(x) - \mathbf{r}(x) + \mathbf{z}_\mathbf{R}(x) + \mathbf{z}_\mathbf{W}(x) + \mathbf{u}(x)\,. \tag{3.36}$$

The distance, $\mathbf{d}$, depends on the normal displacements of the rail centre, $\boldsymbol{\xi}_\mathbf{R}$ and the wheel centre, $\boldsymbol{\xi}_\mathbf{W}$, the combined three-dimensional roughness profile, $\mathbf{r}$, the rail profile, $\mathbf{z}_\mathbf{R}$, the wheel profile, $\mathbf{z}_\mathbf{W}$, and the combined surface displacement, $\mathbf{u}$. All these quantities are organised in vectors of length N_e that contain the values for all element centres. The normal displacements of the wheel centre and the rail centre are independent of the element number and the corresponding vectors of

length N_e are defined as

$$\boldsymbol{\xi}_\mathbf{W}(x) = \xi_\mathrm{W}(x) \begin{bmatrix} 1 \\ 1 \\ \vdots \\ 1 \end{bmatrix} \tag{3.37}$$

$$\boldsymbol{\xi}_\mathbf{R}(x) = \xi_\mathrm{R}(x) \begin{bmatrix} 1 \\ 1 \\ \vdots \\ 1 \end{bmatrix} . \tag{3.38}$$

If the bodies are in contact at a point, the distance is zero; for loss of contact it is positive. A negative value of the distance would mean that the two bodies penetrate into each other, which is physically impossible. At a point where contact occurs, the contact pressure p is positive; at a point with loss of contact, the pressure is zero. Negative contact pressure, which would correspond to the occurrence of adhesion, is excluded. These conditions are summarised as

$$\mathbf{d}(x) \geq \mathbf{0} \tag{3.39}$$

$$\mathbf{p}(x) \geq \mathbf{0} \tag{3.40}$$

$$\mathbf{d}(x)^\mathrm{T}\, \mathbf{p}(x) = 0\,. \tag{3.41}$$

The discrete versions of Equations (3.36) and (3.39)-(3.41) formulated at time step α corresponding to time $(\alpha - 1)\Delta t$ and to wheel centre position on the rail $(\alpha - 1)\Delta x$ read

$$\mathbf{d}(\alpha) = \boldsymbol{\xi}_\mathbf{R}(\alpha) - \boldsymbol{\xi}_\mathbf{W}(\alpha) - \mathbf{r}(\alpha) + \mathbf{z}_\mathbf{R}(\alpha) + \mathbf{z}_\mathbf{W}(\alpha) + \mathbf{u}(\alpha) \tag{3.42}$$

$$\mathbf{d}(\alpha) \geq \mathbf{0} \tag{3.43}$$

$$\mathbf{p}(\alpha) \geq \mathbf{0} \tag{3.44}$$

$$\mathbf{d}(\alpha)^\mathrm{T}\, \mathbf{p}(\alpha) = 0\,. \tag{3.45}$$

Equations (3.31), (3.35) and (3.42)-(3.45) together with Equations (3.8) and (3.14) form a non-linear equation system that completely describes the contact problem at each time step α. This equation system can be solved with the Newton-Raphson method in a similar manner as for the Winkler bedding. The unknown force, $F_\mathrm{n}(\alpha)$, is the root of the function

$$f\left(F_\mathrm{n}(\alpha)\right) = F_\mathrm{n}(\alpha) - \sum_{i=1}^{N_\mathrm{e}} p_i(\alpha)\, A_i\,. \tag{3.46}$$

This root is obtained by iteration

$$F_\mathrm{n}^{[\gamma+1]}(\alpha) = F_\mathrm{n}^{[\gamma]}(\alpha) - \frac{f(F_\mathrm{n}^{[\gamma]}(\alpha))}{f'(F_\mathrm{n}^{[\gamma]}(\alpha))}\,, \tag{3.47}$$

where

$$\begin{aligned} & f'\left(F_{\mathrm{n}}(\alpha)\right) \\ &= \quad \frac{\mathrm{d}\, f\left(F_{\mathrm{n}}(\alpha)\right)}{\mathrm{d}\, F_{\mathrm{n}}(\alpha)} \\ &= \quad 1 - \sum_{i=1}^{N_{\mathrm{e}}} \left\{ \frac{\mathrm{d}\, p_i(\alpha)}{\mathrm{d}\, F_{\mathrm{n}}(\alpha)}\, A_i \right\} . \end{aligned} \tag{3.48}$$

Inserting the inverted version of Equation (3.31)

$$\mathbf{p} = \mathbf{C}^{-1}\,\mathbf{u} = \mathbf{B}\,\mathbf{u} \tag{3.49}$$

$$p_i = \sum_{j=1}^{N_{\mathrm{e}}} B_{ij} u_j\,, \quad i = 1, 2, 3 \ldots N_{\mathrm{e}} \tag{3.50}$$

yields

$$\begin{aligned} & f'\left(F_{\mathrm{n}}(\alpha)\right) \\ &= \quad \frac{\mathrm{d}\, f\left(F_{\mathrm{n}}(\alpha)\right)}{\mathrm{d}\, F_{\mathrm{n}}(\alpha)} \\ &= \quad 1 - \sum_{i=1}^{N_{\mathrm{e}}} A_i \sum_{j=1}^{N_{\mathrm{e}}} B_{ij} \left\{ \frac{\mathrm{d}\, u_j(\alpha)}{\mathrm{d}\, F_{\mathrm{n}}(\alpha)} \right\} . \end{aligned} \tag{3.51}$$

The problem is now that no explicit equation is available for u_j at all points. However, for points that are in contact, the distance d_j is zero and an explicit equation is obtained from Equation (3.42)

$$u_j^{\mathrm{a}}(\alpha) = -\xi_{\mathrm{R}}(\alpha) + \xi_{\mathrm{W}}(\alpha) + r_j(\alpha) - z_{\mathrm{R}j}(\alpha) - z_{\mathrm{W}j}(\alpha)\,. \tag{3.52}$$

It is, however, *a priori* unknown which points are in contact. Therefore, the Newton-Raphson method has to be combined with an active-set strategy [26].

The points that are in contact are called active and form the active set a. As the pressure is zero outside the contact area, the function (3.46) can be rewritten

$$f\left(F_{\mathrm{n}}(\alpha)\right) = F_{\mathrm{n}}(\alpha) - \sum_{i=1}^{N_{\mathrm{a}}} p_i^{\mathrm{a}}(\alpha)\, A_i\,, \tag{3.53}$$

where N_{a} is the number of active points and the derivative reads

$$\begin{aligned} & f'\left(F_{\mathrm{n}}(\alpha)\right) \\ &= \quad 1 - \sum_{i=1}^{N_{\mathrm{a}}} A_i \sum_{j=1}^{N_{\mathrm{a}}} B_{ij}^{\mathrm{a}} \left\{ \frac{\mathrm{d}\, u_j(\alpha)}{\mathrm{d}\, F_{\mathrm{n}}(\alpha)} \right\} . \end{aligned} \tag{3.54}$$

The matrix $\mathbf{C^a} = \mathbf{B^{a-1}}$ is of size $N_\mathrm{a} \times N_\mathrm{a}$ and contains only the influence coefficients of the active points. Inserting consecutively Equation (3.52) and Equations (3.8) and (3.14) results in the following expression for the derivative

$$\begin{aligned} & f'\left(F_\mathrm{n}(\alpha)\right) \\ &= \quad 1 - \sum_{i=1}^{N_\mathrm{e}} A_i \sum_{j=1}^{N_\mathrm{a}} B_{ij}^\mathrm{a} \left\{ \frac{\mathrm{d}}{\mathrm{d}\, F_\mathrm{n}(\alpha)} \left[-\xi_\mathrm{R}(\alpha) + \xi_\mathrm{W}(\alpha) \right] \right\} \\ &= \quad 1 + \left[g_\mathrm{W}(1) + g_\mathrm{R,v}^{v[\alpha-1]\Delta t}(1) \right] \sum_{i=1}^{N_\mathrm{e}} A_i \sum_{j=1}^{N_\mathrm{a}} B_{ij}^\mathrm{a} \,. \end{aligned} \tag{3.55}$$

At iteration step γ in Equation (3.47), the force $F_\mathrm{n}^{[\gamma]}(\alpha)$ has been calculated. To be able to calculate $F_\mathrm{n}^{[\gamma+1]}(\alpha)$, the quantities $\mathbf{p^a}^{[\gamma]}(\alpha)$ and $\mathbf{B^a}^{[\gamma]}$ have to be determined. For this purpose an active set algorithm is applied [2, 26]:

1. The displacements of the wheel centre, ${\xi_\mathrm{W}}^{[\gamma]}(\alpha)$, and rail centre, ${\xi_\mathrm{R}}^{[\gamma]}(\alpha)$, are calculated from Equations (3.8) and (3.14).

2. To determine an initial active set it is assumed that the surface displacement $\boldsymbol{u}(\alpha)$ is zero for all points and the distance is calculated from Equation (3.42):

$$\mathbf{d}(\alpha) = {\boldsymbol{\xi}_\mathbf{R}}^{[\gamma]}(\alpha) - {\boldsymbol{\xi}_\mathbf{W}}^{[\gamma]}(\alpha) - \mathbf{r}(\alpha) + \mathbf{z_R}(\alpha) + \mathbf{z_W}(\alpha) \,. \tag{3.56}$$

   All points with a negative distance, $d_j(\alpha) < 0$, are added to the active set.

3. In order to prevent penetration for the points in the active set, the distance has to be set to zero and the surface displacement $u_j^\mathrm{a}(\alpha)$ is obtained from Equation (3.52)

$$u_j^\mathrm{a}(\alpha) = -\xi_\mathrm{R}^{[\gamma]}(\alpha) + \xi_\mathrm{W}^{[\gamma]}(\alpha) + r_j(\alpha) - z_{\mathrm{R}j}(\alpha) - z_{\mathrm{W}j}(\alpha) \,. \tag{3.57}$$

4. The influence matrix $\mathbf{C}^\mathrm{a} = (\mathbf{B}^\mathrm{a})^{-1}$ containing only the influence coefficients of the points in the active set is constructed.

5. The pressure in the active points is calculated by

$$\mathbf{p^a}(\alpha) = \mathbf{B}^\mathrm{a}\, \mathbf{u^a}(\alpha) \,. \tag{3.58}$$

   All points with negative pressure, $p_j^\mathrm{a} < 0$, are removed from the active set.

6. Steps 3-5 are repeated until no negative pressure is present anymore.

7. The complete pressure vector $\mathbf{p}$ is constructed from $\mathbf{p^a}(\alpha)$ by filling up with zeros for the points that are not in contact and the displacement vector is calculated by

$$\mathbf{u}(\alpha) = \mathbf{C}(\alpha)\, \mathbf{p}(\alpha) \,. \tag{3.59}$$

8. It has to be verified whether the displacement field that was found fulfils Equation (3.43). Therefore, the distance for all points is evaluated with Equation (3.42)

$$\mathbf{d}(\alpha) = \boldsymbol{\xi}_{\mathbf{R}}{}^{[\gamma]}(\alpha) - \boldsymbol{\xi}_{\mathbf{W}}{}^{[\gamma]}(\alpha) - \mathbf{r}(\alpha) + \mathbf{z}_{\mathbf{R}}(\alpha) + \mathbf{z}_{\mathbf{W}}(\alpha) + \mathbf{u}(\alpha)\,. \quad (3.60)$$

   If there are any points with negative distance, $d_j(\alpha) < 0$, these points are added to the active set.

9. Steps 3-8 are repeated until no negative distance is present anymore.

At the end of this iterative procedure, the quantities $\mathbf{p}^{\mathbf{a}[\gamma]}(\alpha)$ and $\mathbf{B}^{\mathbf{a}[\gamma]}$ are known and the force $F_{\mathrm{n}}^{[\gamma+1]}(\alpha)$ can be determined.

To sum up, the Newton-Raphson method is used to solve the non-linear equation system for the contact force $F_{\mathrm{n}}(\alpha)$ at each time step α. At each iteration step of the Newton-Raphson method, an active-set algorithm is applied to determine which points are in contact.

3.5 Inclusion of discrete irregularities

Discrete irregularities such as wheel flats and rail joints can easily be included in the interaction model. For this purpose, the surface profile corresponding to the irregularity, i.e. the wheel or rail profile, is updated in each time step in Equation (3.20) for contact model A, or in Equation (3.42) for contact model B. In *Paper II* this is demonstrated for the case of a wheel flat.

Chapter 4

Applications of the wheel/rail interaction model

This chapter presents some typical results and application areas of the wheel/rail interaction model that has been developed in *Chapter 3*. *Section 4.1* and *4.2* discuss the application of contact model A for the evaluation of the contact-filter effect and for the calculation of impact forces caused by wheel flats, respectively. *Section 4.3* focuses on the possibilities and relative performance of contact models A and B.

4.1 Application of contact model A for the evaluation of the contact-filter effect

In *Paper I*, the contact-filter effect for passing over a rail with sinusoidal corrugation is investigated. The corrugation is assumed to consist of only one sine curve with corrugation wavelength λ and amplitude A. Simulations with contact model A are compared with simulations using a non-linear Hertzian spring as contact model. Contact model A considers the contact-filter effect dynamically, since the bedding model incorporates several springs over the contact-patch length and accounts for a time-variant contact-patch length. Contact model A is therefore said to perform a dynamic roughness filtering. Using the single Hertzian spring, the contact-filter effect has to be accounted for explicitly by calculating an equivalent roughness as a pre-processing step, which is called quasi-static roughness filtering. Three such calculation methods are considered:

- An equivalent roughness is calculated by means of the Winkler bedding depicted in Figure 3.8. Details about the procedure can be found in reference [13].
- An equivalent roughness is obtained by averaging over the nominal contact-patch length (corresponding to the static preload).
- No equivalent roughness is calculated, and the simulations are carried out with the original roughness excitation.

The simulations using contact model A and the Hertzian spring together with the three different methods of quasi-static roughness filtering are compared in Figure 4.1. The results are depicted in form of the maximum contact force as function of the corrugation wavelength, which is passed by the wheel with a speed of $v = 100\,\mathrm{km/h}$. The corrugation amplitudes $10\,\mu\mathrm{m}$ and $100\,\mu\mathrm{m}$ are considered in Figures 4.1(a) and 4.1(b), respectively.

The three distinct peaks occurring in Figure 4.1(b) and to a less clear extent also in Figure 4.1(a) roughly correspond to peaks in the track receptance (see *Paper I*).

The contact-filter effect is clearly noticeable for corrugation wavelengths that are up to three to four times the nominal contact-patch length (the latter being $10.7\,\mathrm{mm}$ for the parameters listed in *Paper I*). In both figures, the curve corresponding to no roughness filtering systematically gives rise to higher contact forces in this wavelength range. This means that considerable errors are made if the contact-filter effect is not considered. However, not much difference is observed between the different methods of roughness filtering in the investigated wavelength range down to $9.3\,\mathrm{mm}$. The simple averaging filtering performs surprisingly well. In Figure 4.1(a) the difference between averaging filtering and dynamic filtering is negligible and in Figure 4.1(b) it reaches slightly over $3\,\mathrm{dB}$ at short wavelengths. No significant difference is observed between quasi-static filtering with the Winkler bedding and dynamic filtering. The results could look substantially different at corrugation wavelengths shorter than the ones considered in Figure 4.1.

As part of future work, the evaluation of the contact-filter effect should be carried out for different sets of measured roughness data. In this case, the results could also look substantially different.

It is also of interest to include contact model B in the comparison in order to evaluate the effect of the roughness profile in lateral direction. Such calculations could indicate in which cases the two-dimensional contact model A is sufficient and in which cases the three-dimensional contact model B should be used. A prerequisite for such a comparison is however the availability of roughness data measured - with sufficient resolution - in longitudinal and lateral direction.

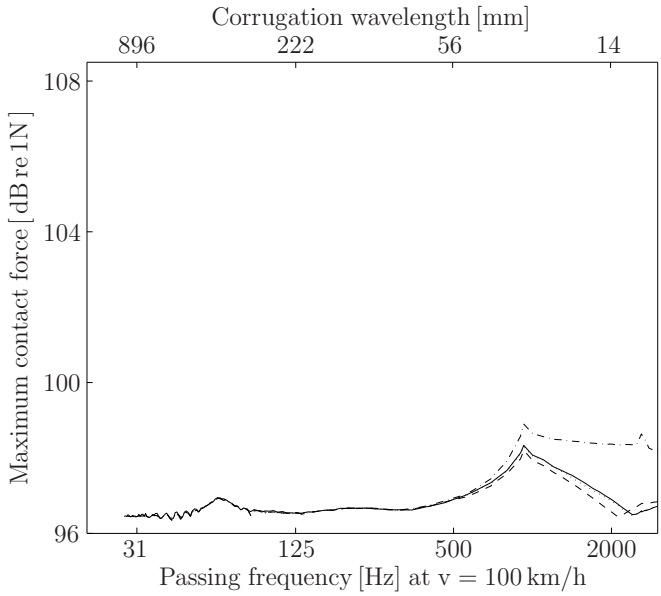

(a) Corrugation amplitude A = 10 μm.

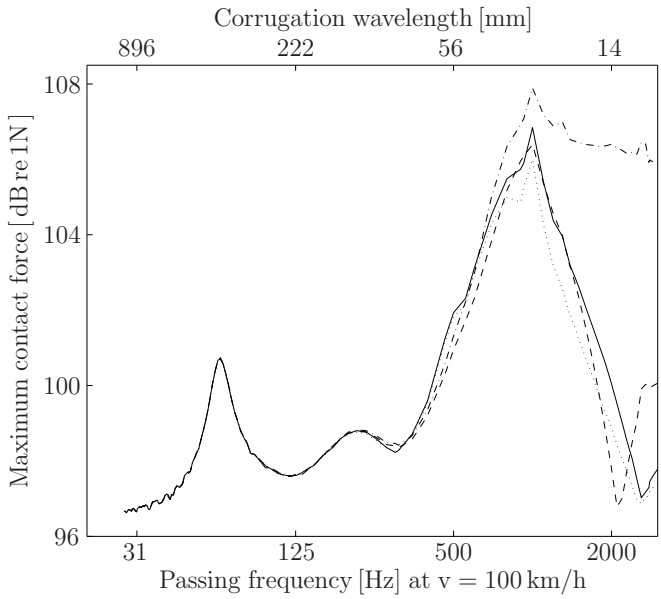

(b) Corrugation amplitude A = 100 μm.

Figure 4.1: Maximum contact force for passing over a rail with sinusoidal corrugation.——— quasi-static roughness filtering with Winkler bedding, – – – quasi-static roughness filtering by averaging, – · – · no roughness filtering, · · · · · · dynamic roughness filtering.

4.2 Application of contact model A for the calculation of impact forces caused by wheel flats

In *Paper II*, the interaction model together with contact model A is applied to calculate impact forces caused by wheel flats. The flat is introduced on a rotating wheel whose profile in the contact zone is updated in every time step. Two kinds of wheel-flat geometries are considered: the newly formed wheel flat with sharp edges as occurring right after formation and the rounded wheel flat, which rapidly develops from the newly formed flat as a result of wheel tread wear and plastic deformation.

To demonstrate the functioning of the modelling approach, simulation results are compared with field measurements from reference [24] in terms of the maximum impact load, see Figure 4.2. In the field test, the impact load caused by a rounded wheel flat with depth $d = 0.9\,\mathrm{mm}$ and length $l = 0.1\,\mathrm{m}$ on a freight train with axle load $24\,\mathrm{t}$ ($P = 117.7\,\mathrm{kN}$) was measured for train speeds between $30\,\mathrm{km/h}$ and $100\,\mathrm{km/h}$. As the receptance of the loaded track in the frequency range of interest could not be measured during the field tests, Nielsen et al. determined rail pad and ballast parameters through model calibration [42]. These model parameters (listed in *Paper II*) are also used in the present simulations. As the calculated impact force varies depending on where the wheel flat hits the rail in relation to the sleeper location, simulations with 40 different initial angular wheel positions are run in order to cover the whole range of maximum impact-force magnitudes. Considering the uncertainty in the track parameters, the level of agreement between simulations and measurements seen in Figure 4.2 is encouraging.

In addition to the maximum forces used for comparison to the field measurements, Figure 4.2 also shows the minimum contact force, allowing identification of loss of contact between wheel and rail. Beside the $0.9\,\mathrm{mm}$ deep rounded wheel flat, also a $0.9\,\mathrm{mm}$ deep new wheel flat is considered. A more detailed description and analysis of Figure 4.2, as well as additional simulation results can be found in *Paper II*. Beside train speed and wheel-flat type, the wheel-flat depth is also identified as important parameter for the magnitude of impact forces caused by wheel flats. Especially at higher train speeds, the impact position of the wheel on the rail in relation to the sleeper location has a significant influence, too.

A minor disadvantage of contact model A, in the context of wheel flats (or other wheel irregularities), is that this contact model requires a reduced wheel radius in order to model Hertzian contact for smooth surfaces. Consequently, the wheel flat has to be mapped onto the reduced wheel implying that it is not possible to represent correctly both wheel-flat depth and length. Though this has not been done yet, it seems promising to apply contact model B to simulate impact forces caused by wheel flats. It would be possible not only to keep the original wheel radius, but also

to include the complete three-dimensional geometry of the wheel flat. This requires however that measurement data of the three-dimensional wheel-flat geometry with sufficient resolution are available.

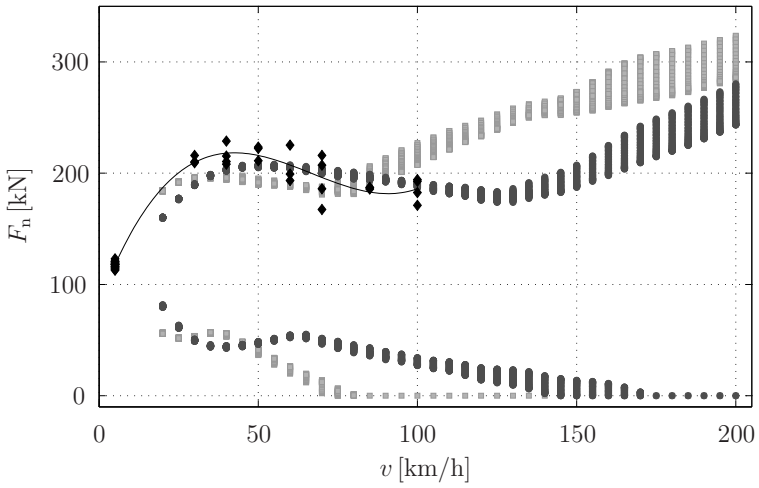

Figure 4.2: Measured maximum impact forces (◇, black) due to a $0.9\,\mathrm{mm}$ deep rounded wheel flat in comparison to calculated maximum and minimum impact forces (○, dark grey). Shown are also a third-degree polynomial fitted to the measured data (——) and calculated results for a $0.9\,\mathrm{mm}$ deep new wheel flat (□, light grey).

4.3 Comparison of contact models A and B

Before comparing contact model A and B as part of the wheel/rail interaction model, the two contact models are investigated separately under static conditions. Contact models A and B are both non-Hertzian models in the sense that they can consider non-Hertzian geometries. In the case of Hertzian profiles of wheel and rail and smooth surfaces, they should result in the same force-deflection characteristic as predicted by the Hertzian theory given in Equation (2.16). Figure 4.3 and Figure 4.4 show the comparison of the force-deflection characteristic of the numerical contact models with their Hertzian counterparts for rail radii of curvature $r_{x_1} = \infty$, $r_{y_1} = 0.30\,\mathrm{m}$ and wheel radii of curvature $r_{x_2} = 0.39\,\mathrm{m}$, $r_{y_2} = \infty$. As contact model A relies on the assumption of a circular contact patch, the rail transverse radius of curvature, r_{y_1}, has been set equal to the wheel rolling-radius, r_{x_2}, in the calculations presented in Figure 4.3. Although the space discretisation $\Delta x = \Delta y = 1\,\mathrm{mm}$ is relatively coarse, the agreement between numerical models and Hertzian theory seen in Figure 4.3 and Figure 4.4 is very good.

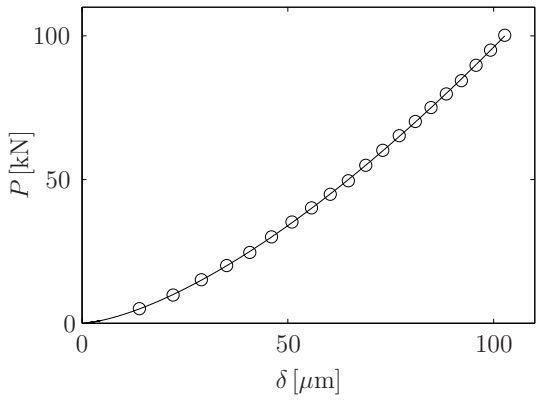

Figure 4.3: Force-deflection characteristic of contact model A (○) in comparison with Hertzian contact (—) for smooth surfaces, $R = 0.39\,\mathrm{m}$ and a spring spacing of $\Delta x = 1\,\mathrm{mm}$.

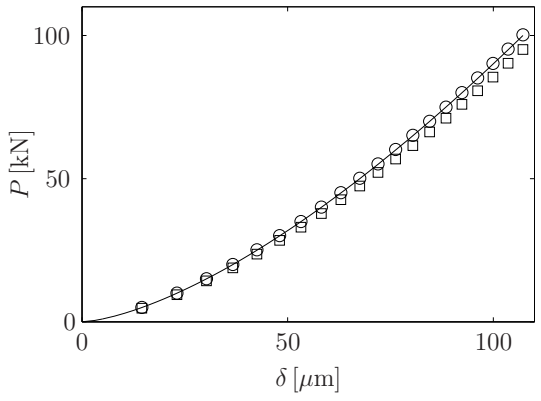

Figure 4.4: Force-deflection characteristic for contact between smooth surfaces: Hertzian contact (—) with radii of curvature $r_{x_1} = \infty$, $r_{y_1} = 0.30\,\mathrm{m}$, $r_{x_2} = 0.39\,\mathrm{m}$, $r_{y_2} = \infty$; contact model B with the space discretisation $\Delta x = \Delta y = 1\,\mathrm{mm}$ using the same Hertzian profiles of wheel and rail (○) and wheel/rail profiles S1002/BV50 (□).

Contact model B can consider the actual transverse profiles of wheel and rail. Figure 4.5 shows the example of a worn S1002 wheel profile on a nominal BV50 rail profile. The force-deflection characteristic of this combination with zero lateral displacement of the wheel on the rail is also represented in Figure 4.4. The contact between the real profiles is slightly less stiff than the contact between the Hertzian surfaces.

For inclusion in contact model B, three-dimensional surfaces, $z_{\mathrm{W}}(x', y')$ and $z_{\mathrm{R}}(x', y')$, are generated from the transverse wheel and rail profiles applying the wheel rolling-radius, r_{x_2}, and the rail radius of curvature in the rolling direction, r_{x_1}. Additionally, the transverse profiles have to be smoothed in order to remove artificial roughness caused by numerical errors in the profile representation. This is done by means of a spline interpolation. The lines of constant distance of the resulting three-dimensional wheel and rail surfaces deviate from the elliptical shapes obtained in the Hertzian case (Figure 4.6), since the transverse radii of curvature are not constant in the case of the real profiles.

Contact models A and B give information about the pressure distribution in the contact zone. An output of contact model A is the force transmitted in each contact spring, which corresponds to the total force transmitted in a strip of the contact zone in the lateral direction with width Δx. The Winkler bedding thus gives an indication about the force distribution in the longitudinal direction, but no information about the distribution in the lateral direction. In the case of smooth surfaces, the longitudinal force distribution obtained with the Winkler bedding is parabolic (see Figure 4.7). Making an assumption about the width of the contact in the lateral direction, a mean pressure distribution in the longitudinal direction could be calculated from the force distribution. In contrast to contact model A, contact model B allows calculating the three-dimensional contact-pressure distribution in the contact zone. The distributions obtained for the case of Hertzian profiles and the case S1002/BV50 under a preload of $P = 65\,\mathrm{kN}$ are presented in Figure 4.9. The longitudinal distribution on the axis $y' = 0$ and the lateral distribution on the axis $x' = 0$ for the same cases in comparison with the elliptical Hertzian distribution from Equation (2.15) is shown in Figure 4.8. The distributions calculated with contact model B for Hertzian profiles agree very well with the theoretical Hertzian distribution. In the case of the real profiles, some differences occur, owing to the non-Hertzian geometry. The maximum contact pressure is 7% higher than in the Hertzian case and the distribution in the lateral direction is slightly asymmetric.

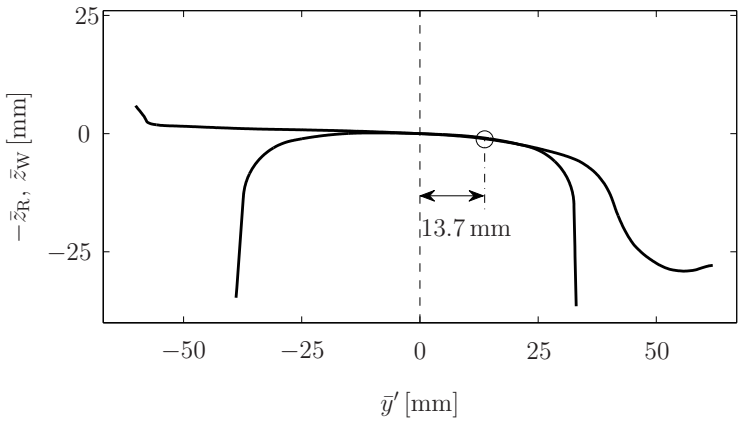

Figure 4.5: Wheel profile S1002 worn over $169\,000\,\mathrm{km}$ on nominal rail profile BV50 with inclination 1:40. The initial contact occurs at $13.7\,\mathrm{mm}$ from the centre line for zero lateral displacement of the wheel on the rail.

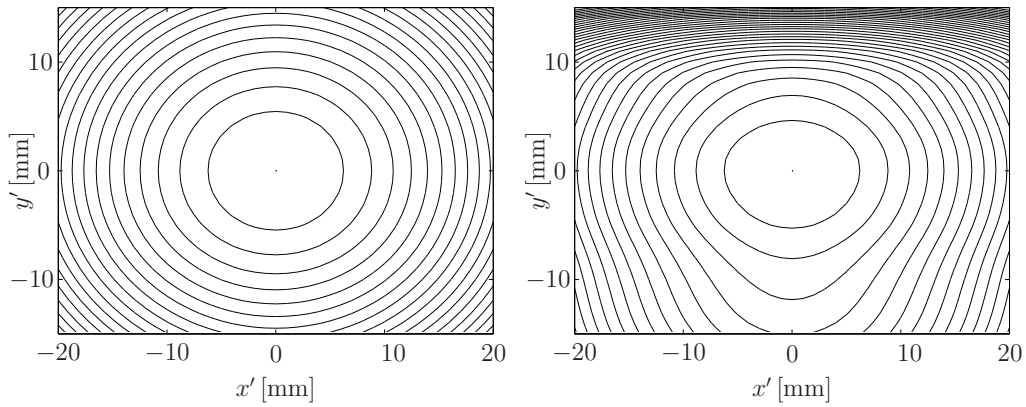

(a) Hertzian profiles of wheel and rail.

(b) Wheel/rail profiles S1002/BV50.

Figure 4.6: Lines of constant distance for the undeformed wheel and rail surfaces with a line spacing of $50\,\mu\mathrm{m}$.

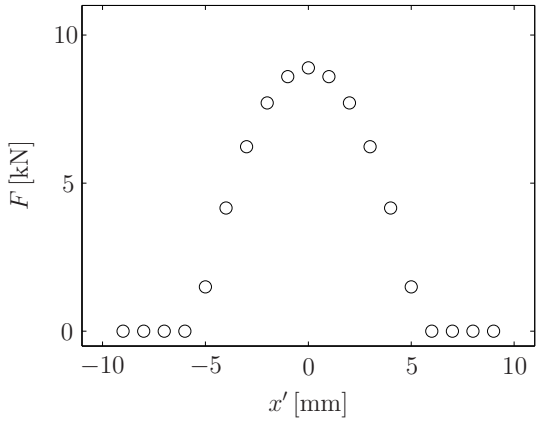

Figure 4.7: Longitudinal force distribution obtained with contact model A for smooth surfaces, $R = 0.39\,\mathrm{m}$, $P = 65\,\mathrm{kN}$ and a spring spacing of $\Delta x = 1\,\mathrm{mm}$.

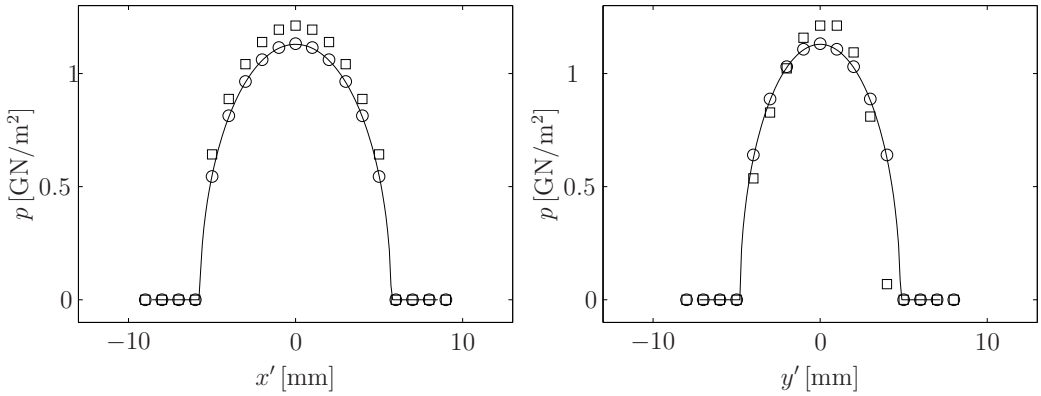

(a) Longitudinal distribution. (b) Lateral distribution.

Figure 4.8: Longitudinal and lateral contact pressure distributions for smooth surfaces: Hertzian contact (—) with radii of curvature $r_{x_1} = \infty$, $r_{y_1} = 0.30\,\mathrm{m}$, $r_{x_2} = 0.39\,\mathrm{m}$, $r_{y_2} = \infty$; contact model B with the space discretisation $\Delta x = \Delta y = 1\,\mathrm{mm}$ using the Hertzian profiles of wheel and rail (○) and wheel/rail profiles S1002/BV50 (□).

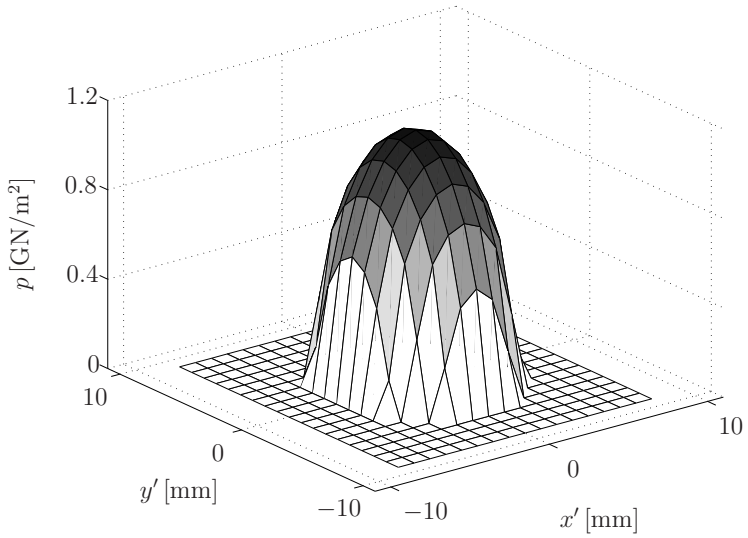

(a) Hertzian profiles of wheel and rail.

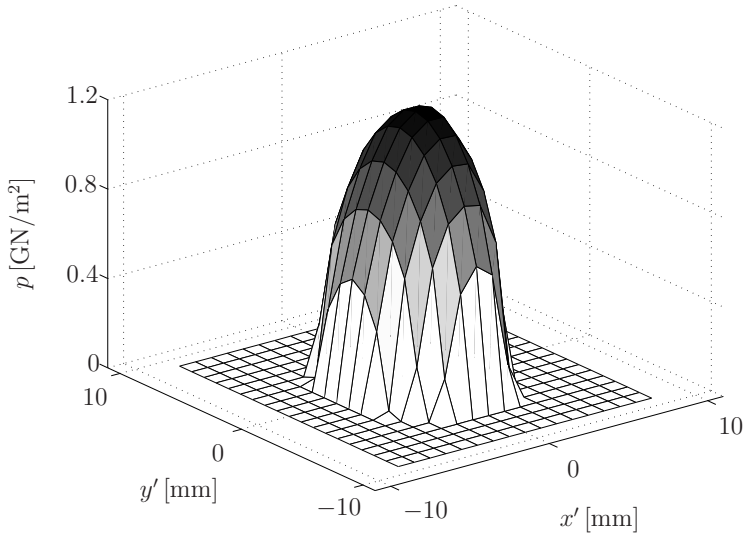

(b) Wheel/rail profiles S1002/BV50.

Figure 4.9: Contact pressure distribution under preload $P = 65\,\mathrm{kN}$ for smooth surfaces calculated with contact model B.

In the following, contact models A and B are considered as part of the wheel/rail interaction model, which is applied with wheel model B.

The first excitation case investigated is parametric excitation caused by the space-dependent stiffness of the track (see Figure 3.6 for the track receptance above a sleeper and at midspan between two sleepers). In this case, the combined wheel and rail roughness, r, is set to zero. The output of the interaction model consists of the time series of the wheel displacement, ξ_{W}, the rail displacement, ξ_{R}, and the total normal contact force, F_{n}. In Figure 4.10 these variables are represented as function of the wheel-centre position on the rail, x, normalised with the sleeper spacing, L_{S}. All three variables appear periodic with the sleeper spacing. The results obtained with contact model A and B are visually identical, except the offset observed for the wheel displacement. The reason for the offset is the different force-deflection characteristics of the contact models. Consequently, the application of the preload, P, leads to different absolute positions of the suspension, $\xi_{\mathrm{S}}(P)$ and the wheel, $\xi_{\mathrm{W}}(P)$. As the wheel is more flexible than the rail, no difference is observed for the rail displacement, $\xi_{\mathrm{R}}(P)$. The visibly identical results for rail displacement and contact force obtained with contact model A and B show that the contact-stiffness difference caused by the non-Hertzian wheel and rail profiles considered in contact model B in comparison to the simplified wheel/rail geometry in contact model A is not significant. The results could look substantially different for a lateral displacement of the wheel on the rail different from zero or for a different wheel or rail profile. Figure 4.10(d) shows the narrow-band spectrum of the contact force with a frequency resolution of $\Delta f = 0.85\,\mathrm{Hz}$, which also agrees well for the two contact models. Before carrying out the Fourier transform, the mean value is subtracted from the signal and a Hanning window is applied. The spectrum shows that the main frequency components of the force signal are the sleeper passing frequency at $43\,\mathrm{Hz}$ and higher harmonics of this frequency.

The second excitation case considered is excitation by roughness. The rail roughness used as input data of the wheel/rail interaction model was measured in the network of Stockholm metro at a curve that shows severe corrugation. The roughness was measured with a Corrugation Analysis Trolley (CAT) [16] in 19 parallel longitudinal lines with a spacing of $1\,\mathrm{mm}$. The sampling distance on each line was $1\,\mathrm{mm}$. In order to remove long roughness wavelengths for which the measurement repeatability was low, the CAT measurement data were low-pass filtered with a cut-off wavelength of $14\,\mathrm{cm}$, which corresponds to an excitation frequency of $200\,\mathrm{Hz}$ at a train speed of $100\,\mathrm{km/h}$. The filter applied was a IIR Butterworth filter of order 20. Figure 4.11(a) shows a sequence of the filtered roughness profile measured on one line over a distance of three sleeper spans. The corresponding three-dimensional roughness profile over the first one and a half sleeper spans is presented in Figure 4.11(b). The roughness profile is dominated by two corrugation wavelengths which occur at approximately $5\,\mathrm{cm}$ and $10\,\mathrm{cm}$. Therefore the

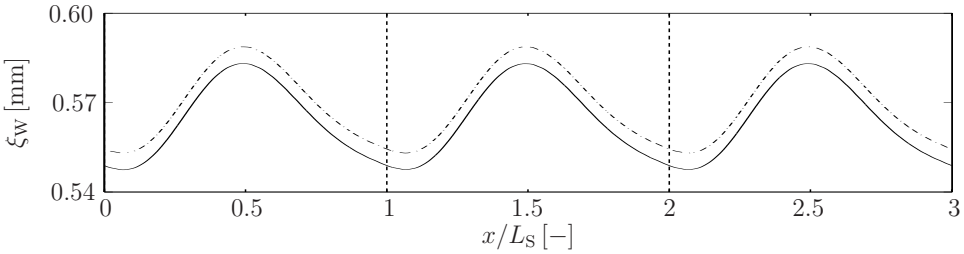

(a) Wheel displacement.

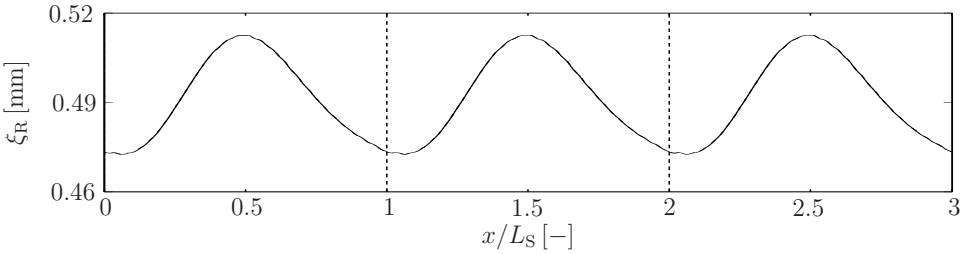

(b) Rail displacement.

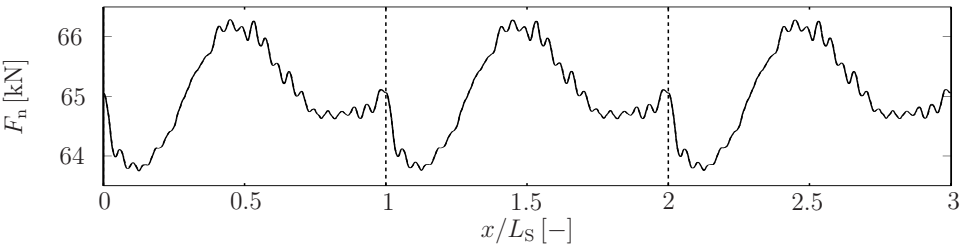

(c) Normal contact force.

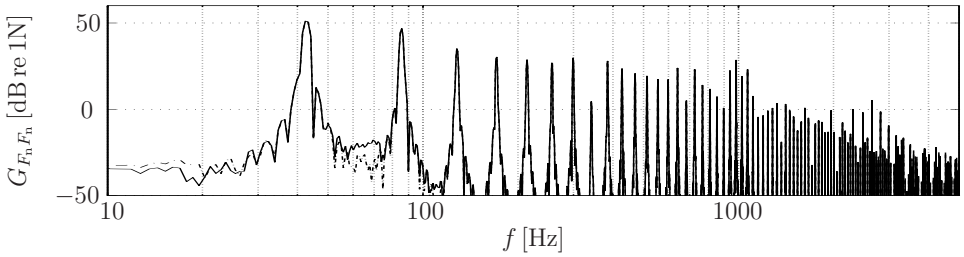

(d) Narrow-band spectrum of the normal contact force.

Figure 4.10: Vertical interaction between smooth wheel and smooth rail due to parametric excitation at train speed $v = 100\,\mathrm{km/h}$ and under preload $P = 65\,\mathrm{kN}$ using contact model A (——) and contact model B ($-\cdot-$).

roughness in parallel longitudinal lines appears strongly correlated, and the three-dimensional roughness profile of the corrugated rail is effectively two-dimensional at wavelengths around the corrugation wavelengths. This is however not the case for shorter wavelengths. Figure 4.12 shows a short section of the roughness profile obtained when each roughness line is low-pass filtered with a cut-off wavelength of $0.9\,\mathrm{cm}$, which corresponds to an excitation frequency of roughly $3\,\mathrm{kHz}$ at a train speed of $100\,\mathrm{km/h}$. The profile appears rather scattered and varies in both longitudinal and lateral directions.

The results of the interaction model for excitation by the roughness from Figure 4.11 are presented in Figure 4.13. Except some small differences occurring for the wheel displacement, contact model A and B give apparently the same results. No significant difference can be observed for the rail displacement and the normal contact force in Figure 4.13. The reason for this is the effectively two-dimensional roughness profile mentioned above. However, it cannot be concluded from these results that contact models A and B will also give the same results for a different type of roughness data. Especially when the roughness in parallel lines is highly uncorrelated, significant differences are expected. Such calculations have not yet been carried out, since the required roughness data were not available.

A frequency analysis of the contact-force signal from the simulations presented in Figure 4.13 corroborates the expectation of differences between the contact models for a more uncorrelated roughness. Figure 4.14(a) shows the narrow-band spectrum of the contact force calculated in the same manner as mentioned in the paragraph about the first excitation case. The spectrum shows peaks corresponding to the corrugation wavelengths around $270\mathrm{Hz}$ and $530\mathrm{Hz}$, at the sleeper passing frequency, $f_\mathrm{S} = 43\,\mathrm{Hz}$, and at higher harmonics of the three frequencies. The third-octave band spectrum presented in Figure 4.14(c) reveals that the energy content of the force signals obtained for the two contact models is identical in the frequency range $80\,\mathrm{Hz} - 1\,\mathrm{kHz}$. At higher frequencies, especially above $2.5\,\mathrm{kHz}$, significant differences occur (see also Figure 4.14(b)). In the band with mid-frequency $4\,\mathrm{kHz}$, contact model B gives a contact-force level of more than $8\,\mathrm{dB}$ lower than contact model A. This can be explained by the highly uncorrelated roughness at short wavelengths depicted in Figure 4.12. Differences in the third-octave band spectra occur also at frequencies lower than $80\,\mathrm{Hz}$. In spite of the low-pass filtering of the roughness, this might be due to uncorrelated, long-wavelength components in the roughness signals. Since the applied filter is not perfect, the amplitudes of these components have indeed been reduced considerably, but not eliminated completely.

Figure 4.15 shows the force distribution in the contact zone obtained for the wheel/rail interaction excited by the roughness from Figure 4.11. Depicted is the force distribution in the longitudinal direction (on axis x') and lateral direction (on axis y') as a function of the wheel-centre position on the rail, x (normalised with the sleeper spacing L_S). The longitudinal force distribution in the contact zone is a direct re-

sult from contact model A (Figure 4.15(a)). For contact model B, the distributions have been calculated from the three-dimensional pressure distribution by integration over lateral strips to obtain the longitudinal force distribution (Figure 4.15(b)), and over longitudinal strips to obtain the lateral force distribution (Figure 4.15(c)). The figures do not only give information about the force distributions, but also show how the contact zone migrates under the wheel centre located at $x' = 0$ and $y' = 0$. Although the total normal contact force obtained for contact models A and B (Figure 4.13(c)) is identical, some differences can be seen in the longitudinal force distributions presented in Figures 4.15(a) and 4.15(b). Figure 4.15(c) reveals that the lateral force distribution is strongly cleft. This can also be seen in Figure 4.16, which shows the three-dimensional pressure distribution for two selected wheel positions.

It has been shown that the three-dimensional contact model B has advantages over the two-dimensional contact model A. The actual three-dimensional geometry of wheel and rail and the roughness throughout the whole contact area are considered in contact model B and the three-dimensional contact-pressure distribution is obtained at each time step. It is, however, also important how contact model B performs in comparison to contact model A concerning computational efficiency. In order to obtain the spectra in Figure 4.14(a) with good frequency resolution, the wheel/rail interaction has been calculated over a distance of $36\,\mathrm{m}$, which corresponds to a simulated time of $1.3\,\mathrm{s}$ at a train speed of $v = 100\,\mathrm{km/h}$. Using the two-dimensional contact model A, this calculation takes less than two minutes (on an iMac with Intel Core Duo 2.0 GHz processor), provided that the moving Green's functions of the track have been pre-calculated. This results in a ratio of about 100 between calculation time and simulated time. Using the three-dimensional contact model B, the same calculation takes slightly less than 20 minutes, which results in a ratio of approximately 1000 between calculation time and simulated time. This can still be considered as computationally efficient.

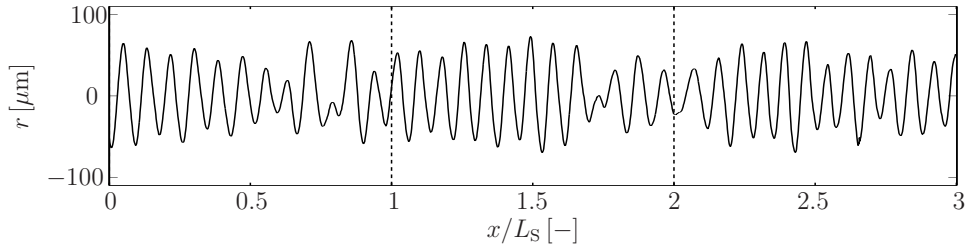

(a) Roughness profile in one longitudinal line.

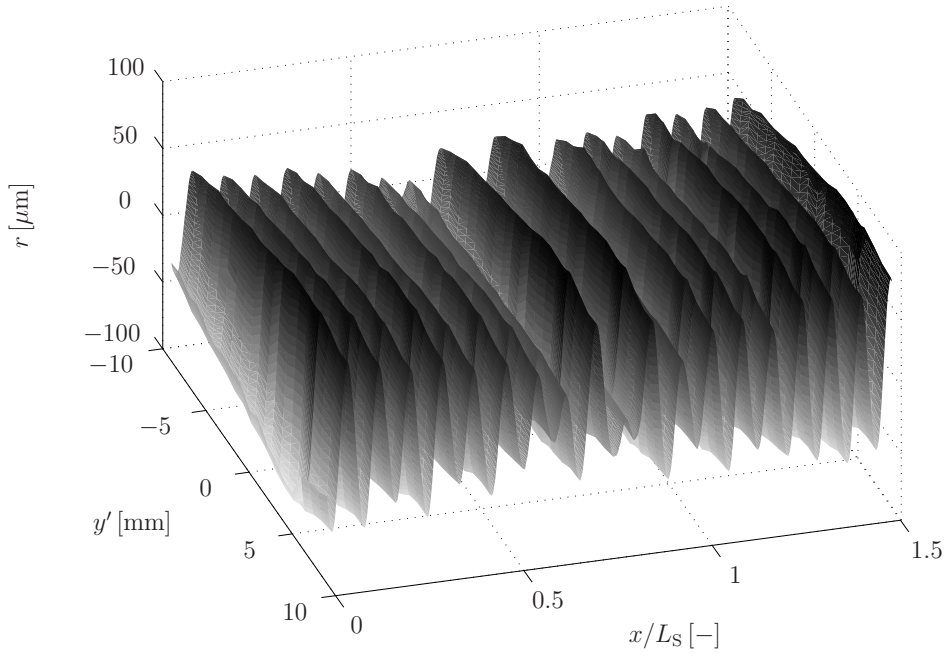

(b) Roughness profile in 19 longitudinal lines with spacing $1\,\mathrm{mm}$.

Figure 4.11: Measured rail roughness low-pass filtered with cut-off wavelength $14\,\mathrm{cm}$.

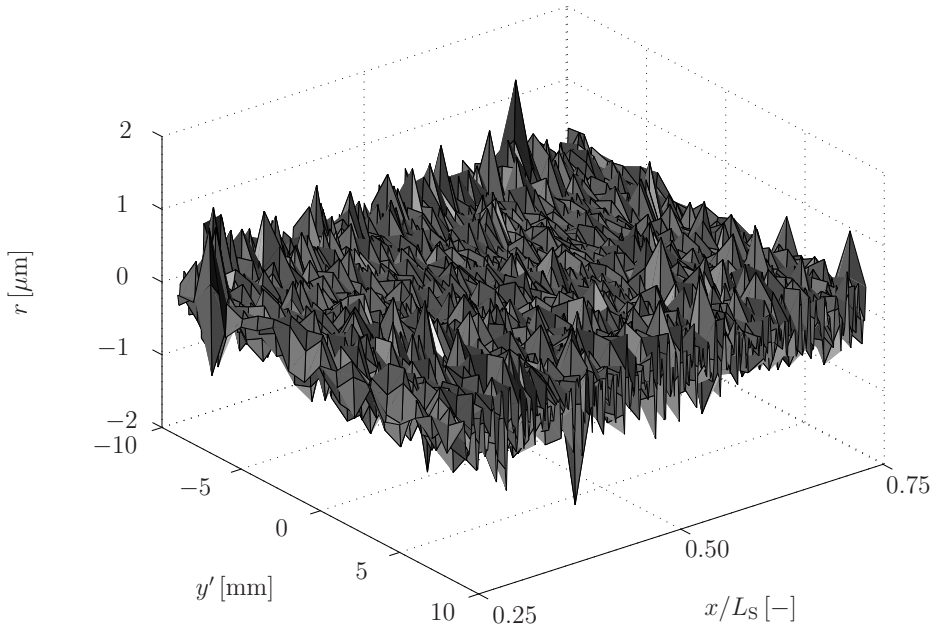

Figure 4.12: Measured rail roughness low-pass filtered with cut-off wavelength $0.9\,\mathrm{cm}$ in 19 parallel longitudinal lines.

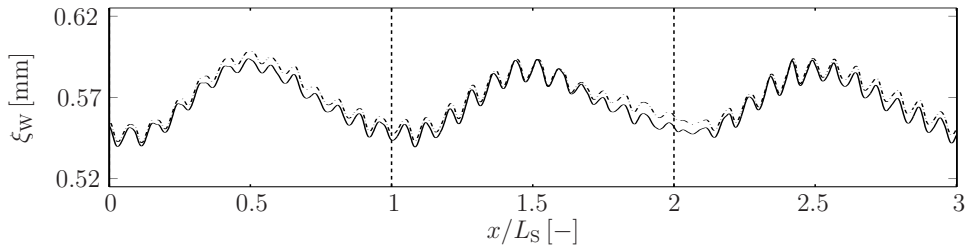

(a) Wheel displacement.

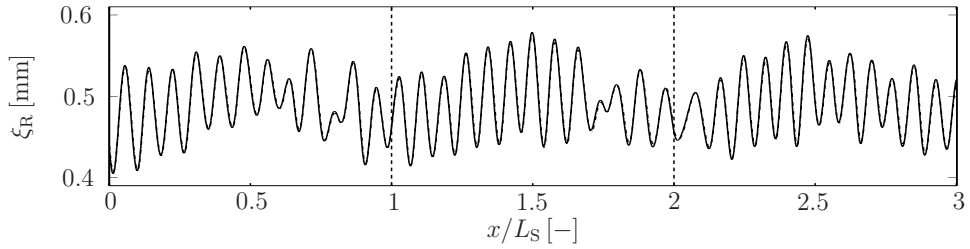

(b) Rail displacement.

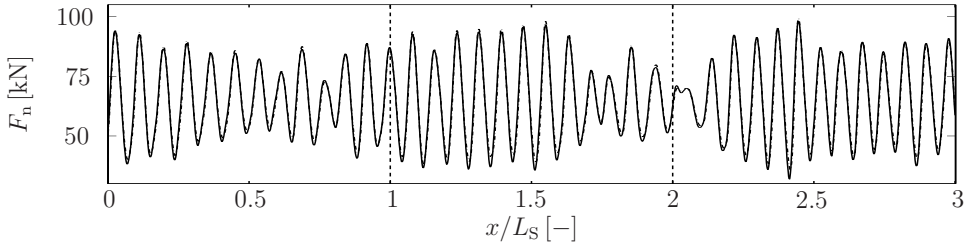

(c) Normal contact force.

Figure 4.13: Vertical interaction between smooth wheel and corrugated rail at train speed $v = 100\,\mathrm{km/h}$ and under preload $P = 65\,\mathrm{kN}$ using contact model A (——) and contact model B ($-\cdot-$).

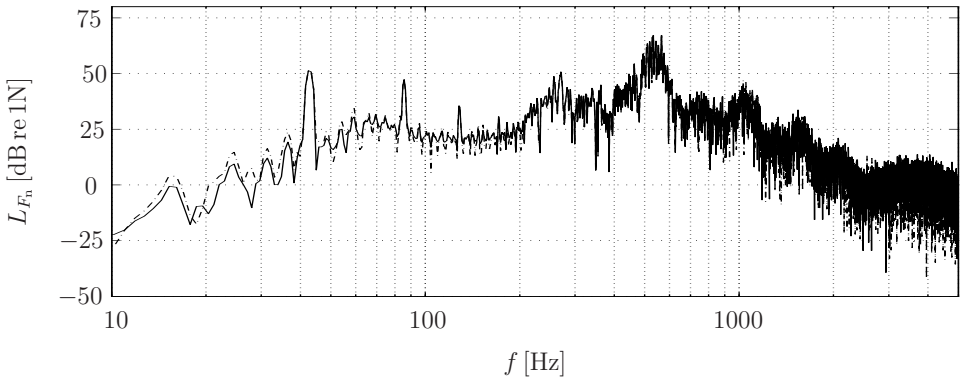

(a) Narrow-band spectrum of the normal contact force in the range $10\,\mathrm{Hz} - 5\,\mathrm{kHz}$.

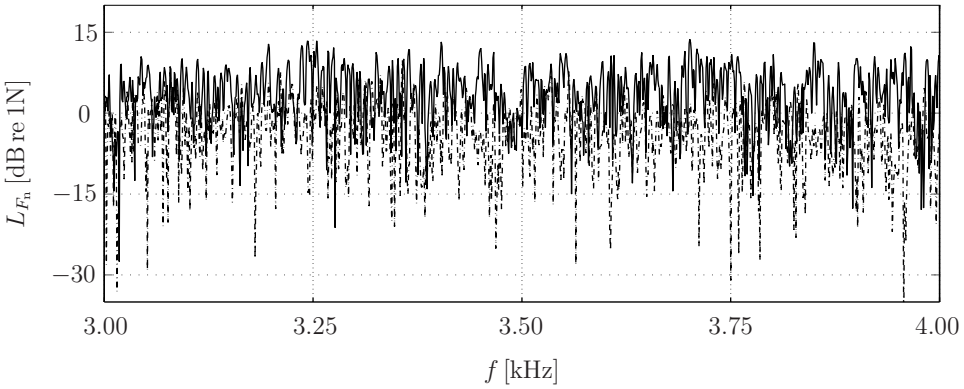

(b) Narrow-band spectrum of the normal contact force in the range $3\mathrm{kHz} - 4\mathrm{kHz}$.

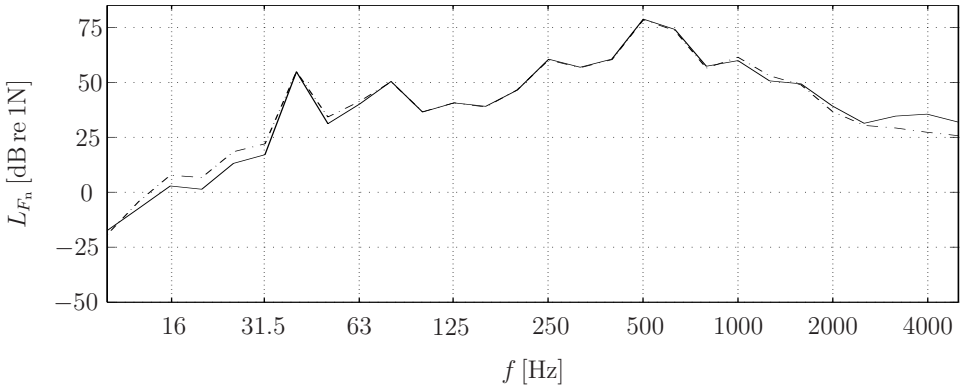

(c) Third-octave band spectrum of the normal contact force.

Figure 4.14: Vertical interaction between smooth wheel and corrugated rail at train speed $v = 100\,\mathrm{km/h}$ and under preload $P = 65\,\mathrm{kN}$ using contact model A (——) and contact model B ($- \cdot -$): spectral analysis of the contact force.

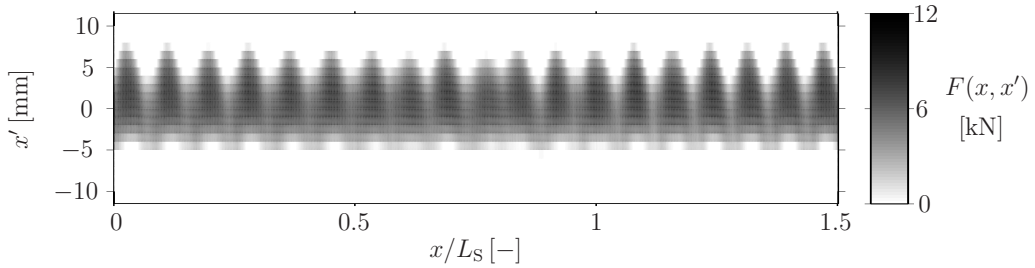

(a) Longitudinal distribution of the normal force, contact model A.

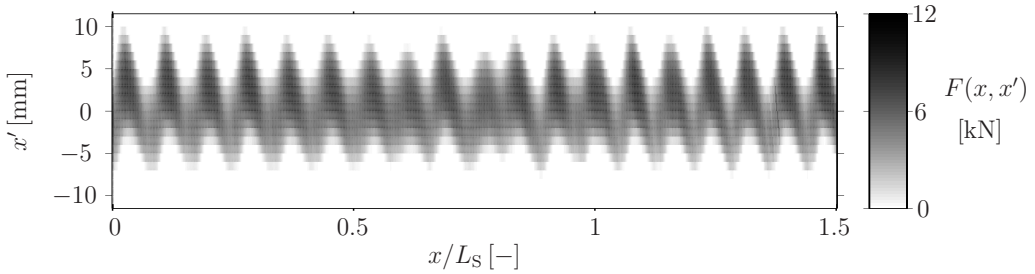

(b) Longitudinal distribution of the normal force, contact model B.

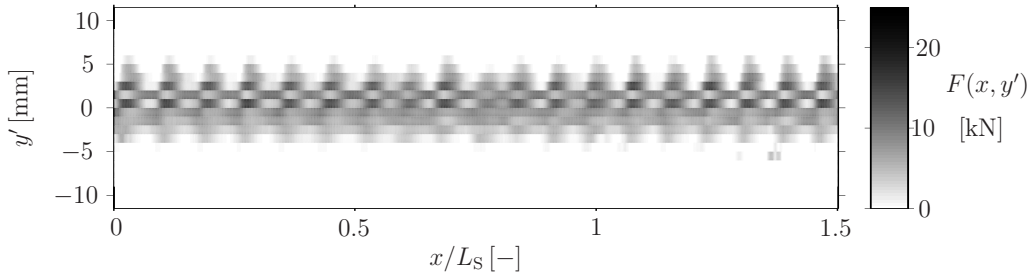

(c) Lateral distribution of the normal force, contact model B.

Figure 4.15: Vertical interaction between smooth wheel and corrugated rail at train speed $v = 100\,\mathrm{km/h}$ and under preload $P = 65\,\mathrm{kN}$ using contact model A and contact model B: comparison of force distributions in the contact zone.

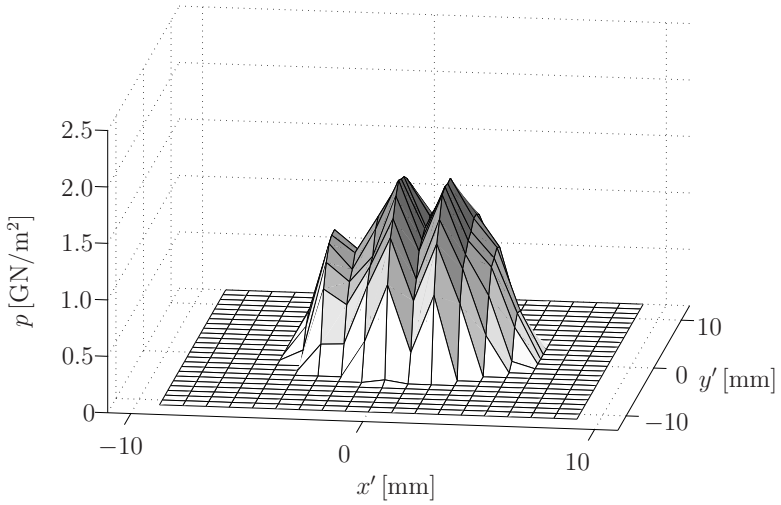

(a) Wheel position $x/L_\mathrm{S} = 1.01$.

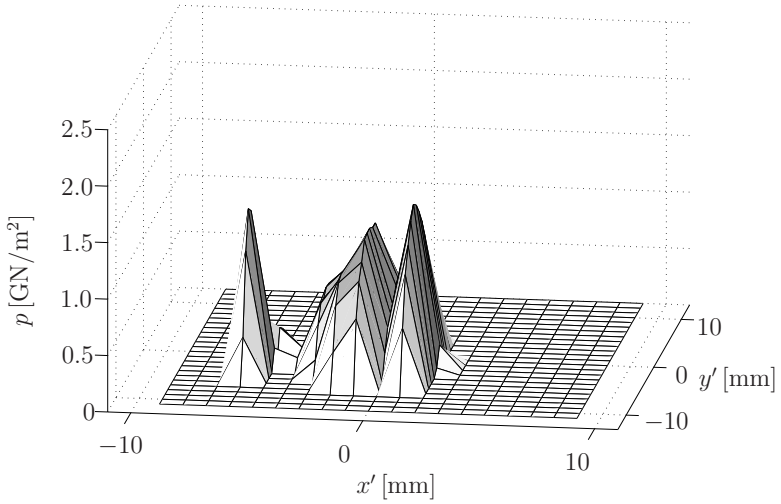

(b) Wheel position $x/L_\mathrm{S} = 1.37$.

Figure 4.16: Vertical interaction between smooth wheel and corrugated rail at train speed $v = 100\,\mathrm{km/h}$ and under preload $P = 65\,\mathrm{kN}$ using contact model B: contact pressure distribution for two selected wheel positions.

Chapter 5
Conclusions and future work

5.1 Conclusions

In this thesis, a time-domain model for vertical wheel/rail interaction has been presented, which accounts for the non-linear processes in the contact zone.

An important feature of the model is the representation of wheel and track by Green's functions, which allows inclusion of any linear wheel and track model. A discretely supported rail, for instance, can easily be considered. As the Green's functions are pre-calculated before starting the dynamic simulations, the modelling approach leads to high computational efficiency. Consequently, detailed contact models can be included. Two non-Hertzian contact models have been introduced in this thesis. The first contact model is a two-dimensional (2D) model consisting of a Winkler bedding of independent springs. This model uses a simplified wheel and rail geometry and takes into account one line of wheel/rail roughness in the rolling direction. The second contact model is a three-dimensional (3D) model based on an influence-function method for the elastic half-space. This model considers the real three-dimensional wheel and rail geometry and includes the roughness in several parallel lines. Both contact models include the contact-filter effect dynamically and do not require the calculation of an equivalent roughness as pre-processing step. Moreover, discrete irregularities such as wheel flats and rail joints can readily be included by updating the wheel or rail profile in the contact zone in each time step.

In the thesis and the appended papers, the wheel/rail interaction model has been applied for different excitation cases. Cases considered are parametric excitation due to the space-dependent stiffness on a discretely supported rail, excitation by an idealised sinusoidal and by measured roughness of the wheel and rail running surfaces, and excitation by different types of wheel flats. Some specific conclusions can be drawn from these simulations:

In *Paper I*, the contact-filter effect has been evaluated for passing over a rail with idealised sinusoidal roughness. Simulations have been carried out with (1) the 2D contact model and (2) a Hertzian spring as contact model applied in combination with an equivalent roughness calculated in a pre-processing step. The contact-filter

effect was clearly visible for roughness wavelengths that were up to three to four times the nominal contact-patch length. However, no significant difference was observed between the results based on dynamic roughness filtering and quasi-static roughness filtering, performed in case (1) and case (2) respectively. The results could look substantially different, if the same investigation was carried out for measured wheel and rail roughness.

In *Paper II*, the interaction model together with the 2D contact model has been applied to calculate impact forces caused by wheel flats. Simulation results have been compared to field measurements in terms of the maximum impact forces during wheel-flat passage. The agreement found between simulations and measurements was fairly good throughout the investigated range of train speeds from $30\,\mathrm{km/h}$ to $100\,\mathrm{km/h}$. The short parameter study presented in *Paper II* showed that train speed, wheel-flat depth and wheel-flat type are important parameters for the magnitude of the impact force. Especially for higher train speeds, the impact position of the wheel on the rail in relation to the sleeper location has a significant influence, too. A minor disadvantage of the 2D contact model in the context of wheel flats (or other wheel irregularities) is that this contact model requires a reduced wheel radius in order to model Hertzian contact for smooth surfaces. Consequently, the wheel flat has to be mapped onto the reduced wheel, implying that it is not possible to represent correctly both wheel-flat depth and length. Using the 3D contact model would make it possible to keep the original wheel radius and to include the complete three-dimensional geometry of the wheel flat.

In *Section 4.3*, a comparison has been made between the 2D and 3D contact models. The 3D contact model is clearly superior to the 2D model in terms of the information obtained about the dynamic processes in the contact zone. The three-dimensional contact pressure distribution is calculated in every time step, while the 2D contact model gives only information about the force distribution in the spring bedding in the rolling direction. The 3D contact model requires, however, longer calculation times than the 2D model. In the example evaluated in *Section 4.3*, the calculation times differed by a factor of 10. With regard to the absolute calculation time, the interaction model using the 3D contact model can still be considered as computationally efficient. The results of the interaction model using the 2D and 3D contact models have been compared in *Section 4.3* for (a) parametric excitation on a discretely supported rail and for (b) excitation by a measured rail roughness. In case (a), the two contact models give visually identical results concerning the time series of the total normal contact force. This shows that the contact-stiffness difference caused by the non-Hertzian wheel and rail profiles considered in the 3D contact model in comparison to the simplified wheel/rail geometry in the 2D model is not significant. It should be noted that only one example has been calculated. The results could look substantially different for a different lateral displacement of the wheel on the rail or for a different wheel or rail profile. In case (b), the results ob-

tained with the two contact models in terms of the total normal contact force were also very similar. This can be attributed to the fact that the measured roughness data used as excitation show a distinctive corrugation pattern and the roughness profile is essentially two-dimensional. A frequency analysis of the contact force revealed, however, that differences of more than $8\,\mathrm{dB}$ occurred at higher frequencies between the results of the two contact models. This can be explained by a low degree of correlation between roughness across the width of the contact patch in the corresponding wavelength range. These results suggest that the application of the 3D contact model is preferable when the degree of correlation between roughness across the width of the contact patch is low. More simulations with different sets of measured roughness should nevertheless be carried out before drawing a final conclusion.

Summing up, the functioning of the developed vertical wheel/rail interaction model has been demonstrated for a variety of excitation cases. The model allows considering the three-dimensional roughness distribution throughout the contact patch, the real non-Hertzian wheel/rail geometry, and comprehensive wheel and track models. The simulation results give detailed information about the dynamic processes in the contact zone. The applicability of the interaction model for practical cases depends, however, on the availability and accuracy of input data. Critical are, for instance, the parameters of the track model characterising railpads and ballast and the wheel/rail roughness distribution. Only one set of three-dimensional rail-roughness data was available for the simulations in this thesis.

5.2 Future work

Aspects of future work have already been mentioned throughout the thesis and are briefly summarised here.

Regarding the vertical interaction model, future work primarily concerns the application of the model. The overall aim of this thesis was to develop the interaction model and to demonstrate its functioning. The model has not yet been applied for extensive parameter studies and investigations of phenomena. One such area of application is the evaluation of the contact-filter effect for different sets of measured roughness data. Simulations carried out with the 2D contact model should be compared with simulations using a Hertzian spring as contact model in combination with quasi-static roughness filtering. It is also of interest to include the 3D contact model in the comparison in order to evaluate correlation effects across the contact width and carry on the comparison between the 2D and 3D contact models. In order to obtain the required input data, additional roughness measurements should be carried out. Another such area of application area is the investigation of impact forces caused by wheel flats. Here, a more detailed parameter study should be conducted, including also the three-dimensional contact model.

Moreover, additional validation of the interaction model against field measurements should be sought. In *Paper II*, it has been shown that the simulation results from the model agree well with one set of measured impact forces caused by wheel flats. To gain confidence that the developed model is quantitatively reliable, a more extensive comparison to field measurements should be carried out.

However, the main aspect of future work is to extend the model by including tangential wheel/rail interaction. An outline of the procedure intended to follow is given in *Paper I*. The ultimate aim is thus to obtain a model for the combined vertical and tangential wheel/rail interaction that serves as a basis for the prediction of rolling noise, impact noise and squeal noise.

Bibliography

[1] A. Alonso and J.G. Giménez. Wheel-rail contact: Roughness, heat generation and conforming contact influence. *Tribology International*, 41:755–768, 2008.

[2] P. Andersson. *Modelling Interfacial Details in Tyre/Road Contact - Adhesion Forces and Non-Linear Contact Stiffness*. PhD Thesis, Applied Acoustics, Chalmers University of Technology, Göteborg, Sweden, 2005.

[3] J.-B. Ayasse and H. Chollet. Determination of the wheel rail contact patch in semi-Hertzian conditions. *Vehicle System Dynamics*, 43(3):161–172, 2005.

[4] J.-B. Ayasse and H. Chollet. Wheel-rail contact. In S. Iwnicki, editor, *Handbook of Railway Vehicle Dynamics*, chapter 4. CRC Press, Taylor and Francis Group, Boca Raton, FL, 2006.

[5] L. Baeza, A. Roda, J. Carballeira, and E. Giner. Railway train-track dynamics for wheelflats with improved contact models. *Nonlinear Dynamics*, 45:385–397, 2006.

[6] J. Boussinesq. *Application des Potentiels à l'Étude de l'Équilibre et du Mouvement des Solides Élastiques.* Gauthier-Villars, Paris, 1885.

[7] F. Bucher, K. Knothe, and A. Theiler. Normal and tangential contact problem of surfaces with measured roughness. *Wear*, 253:204–218, 2002.

[8] V. Cerruti. *Mem. fis. mat.* Accademia dei Lincei, Roma, 1882.

[9] R.A. Clark, P.A. Dean, J.A. Elkins, and S.G. Newton. An investigation into the dynamic effects of railway vehicles running on corrugated rails. *Journal of Mechanical Engineering Science*, 24(2):65–76, 1982.

[10] S. Damme, U. Nackenhorst, A. Wetzel, and B.W. Zastrau. On the numerical analysis of the wheel-rail system in rolling contact. In K. Popp and W. Schiehlen, editors, *System Dynamics and Long-Term Behaviour of Railway Vehicle, Track and Subgrade*, volume 6 of *Lecture Notes in Applied Mechanics*. Springer-Verlag, Berlin Heidelberg, 2003.

[11] M.G. Dittrich and X. Zhang. The harmonoise/imagine model for traction noise of powered railway vehicles. *Journal of Sound and Vibration*, 293:986–994, 2006.

[12] J.M. Fields and J.G. Walker. Comparing the relationships between noise level and annoyance in different surveys: A railway noise vs. aircraft and road traffic comparison. *Journal of Sound and Vibration*, 81(1):51–80, 1982.

[13] R.A.J. Ford and D.J. Thompson. Simplified contact filters in wheel/rail noise prediction. *Journal of Sound and Vibration*, 293:807–818, 2006.

[14] P.-E. Gautier, C. Talotte, and P. Fodiman. La recherche à la SNCF pour la réduction du bruit des trains. *Revue générale des chemins de fer*, 6:9–19, 1999.

[15] S.L. Grassie, R.W. Gregory, D. Harrison, and K.L. Johnson. The dynamic response of railway track to high frequency vertical excitation. *Journal of Mechanical Engineering Science*, 24(2):77–90, 1982.

[16] S.L. Grassie, M.J. Saxon, and J.D. Smith. Measurement of longitudinal rail irregularities and criteria for acceptable grinding. *Journal of Sound and Vibration*, 227(5):949–964, 1999.

[17] J.A. Greenwood and J.H. Tripp. The elastic contact of rough spheres. *ASME Journal of Applied Mechanics*, 34:153–159, 1967.

[18] J.A. Greenwood and J.B.P. Williamson. Contact of nominally flat surfaces. *Proceedings of the Royal Society of London. Series A, Mathematical and Physical Sciences*, 295(1442):300–319, 1966.

[19] L. Gry. Dynamic modelling of railway track based on wave propagation. *Journal of Sound and Vibration*, 195(3):477–505, 1996.

[20] M. Heckl. Proposal for a railway simulation program. In *A Workshop on Rolling Noise Generation*, pages 128–148. Institut für Technische Akustik, Technische Universität Berlin, October 1989.

[21] K. Hempelmann, F. Hiss, K. Knothe, and B. Ripke. The formation of wear patterns on rail tread. *Wear*, 144(1-2):179–195, 1991.

[22] H. Hertz. Ueber die Berührung fester elastischer Körper. *Journal für reine und angewandte Mathematik*, 92:156–171, 1882.

[23] J. Jergéus. Railway wheel flats - martensite formation, residual stresses, and crack propagation. PhD Thesis, Division of Solid Mechanics, Chalmers University of Technology, Göteborg, Sweden, 1998.

[24] A. Johansson and J.C.O. Nielsen. Out-of-round railway wheels - wheel-rail contact forces and track response derived from field tests and numerical simulations. *Proc IMechE, Part F: Journal of Rail and Rapid Transport*, 217:135–146, 2003.

[25] K.L. Johnson. *Contact mechanics*. Cambridge University Press, 1987.

[26] J.J. Kalker. *Three-Dimensional Elastic Bodies in Rolling Contact*. Kluwer Academic Publishers, Dordrecht, Boston, London, 1990.

[27] J.J. Kalker. Wheel-rail rolling contact theory. *Wear*, 144:243–261, 1991.

[28] K. Knothe and S. Stichel. *Schienenfahrzeugdynamik*. Springer-Verlag, Berlin Heidelberg, 2003.

[29] K. Knothe, R. Wille, and W. Zastrau. Advanced contact mechanics - road and rail. *Vehicle System Dynamics*, 35(4-5):361–407, 2001.

[30] KL. Knothe and S.L. Grassie. Modelling of railway track and vehicle/track interaction at high frequencies. *Vehicle System Dynamics*, 22:209–262, 1993.

[31] H. Le-The. *Normal- und Tangentialspannungsberechnung beim rollenden Kontakt für Rotationskörper mit nichtelliptischen Kontaktflächen*. Fortschrittberichte VDI, Reihe 12: Verkehrstechnik/Fahrzeugtechnik, Nr.87. VDI-Verlag GmbH, Düsseldorf, 1987.

[32] Ch. Linder. *Verschleiss von Eisenbahnrädern mit Unrundheiten.* PhD thesis, Dissertation ETH, Nr.12342, 1997.

[33] G. Lundberg and H. Sjövall. Stress and deformation in elastic contacts. Publikation nr 4, The Institution of Theory of Elasticity and Strength of Materials, Chalmers University of Technology, Gothenburg, Sweden, 1958.

[34] T. Mazilu. Green's functions for analysis of dynamic response of wheel/rail to vertical excitation. *Journal of Sound and Vibration*, 306:31–58, 2007.

[35] H.C. Meacham and D.R. Ahlbeck. A computer study of dynamic loads caused by vehicle-track interactions. *ASME Journal of Engineering for Industry*, 91:808–816, 1969.

[36] U. Moehler. Community response to railway noise: A review of social surveys. *Journal of Sound and Vibration*, 120(2):321–332, 1988.

[37] L. Nayak and K.L. Johnson. Pressure between elastic bodies having a slender area of contact and arbitrary profiles. *International Journal of Mechanical Sciences*, 21(4):237–247, 1979.

[38] S.G. Newton and R.A. Clark. An investigation into the dynamic effects on the track of wheelflats on railway vehicles. *Journal of Mechanical Engineering Science*, 21(4):287–297, 1979.

[39] J.C.O. Nielsen. Dynamic interaction between wheel and track - a parametric search towards an optimal design of rail structures. *Vehicle System Dynamics*, 23(2):115 – 132, 1994.

[40] J.C.O Nielsen. High-frequency vertical wheel-rail contact forces - validation of a prediction model by field testing. In *Proceedings of the 7th International Conference on Contact Mechanics and Wear of Rail/Wheel Systems*, Brisbane, Australia, September 2006.

[41] J.C.O Nielsen and A. Igeland. Vertical dynamic interaction between train and track - influence of wheel and track imperfections. *Journal of Sound and Vibration*, 187(5):825–839, 1995.

[42] J.C.O. Nielsen, J.W. Ringsberg, and L. Baeza. Influence of railway wheel flat impact on crack growth in rails. In *Proceedings of the 8th International Heavy Haul Conference*, pages 789–797, Rio de Janeiro, Brazil, 14-16 June 2005.

[43] A. Nordborg. Wheel/rail noise generation due to nonlinear effects and parametric excitation. *Journal of the Acoustical Society of America*, 111(4):1772–1781, April 2002.

[44] J.P. Pascal and G. Sauvage. The available methods to calculate the wheel/rail forces in non Hertzian contact patches and rail damaging. *Vehicle System Dynamics*, 22:263–275, 1993.

[45] B. Paul and J. Hashemi. Contact pressures on closely conforming elastic bodies. *Journal of Applied Mechanics*, 48(3):543–548, 1981.

[46] J. Piotrowski and H. Chollet. Wheel-rail contact models for vehicle system dynamics including multi-point contact. *Vehicle System Dynamics*, 43(6-7):455–483, 2005.

[47] J. Piotrowski and W. Kik. A simplified model of wheel/rail contact mechanics for non-Hertzian problems and its application in rail vehicle dynamics. *Vehicle System Dynamics*, 46(1-2):27–48, 2008.

[48] P. Remington and J. Webb. Estimation of wheel/rail interaction forces in the contact area due to roughness. *Journal of Sound and Vibration*, 193(1):83–102, 1996.

[49] P.J. Remington. Wheel/rail noise - Part I: Characterization of the wheel/rail dynamic system. *Journal of Sound and Vibration*, 46(3):359–379, 1976.

[50] P.J. Remington. Wheel/rail noise - Part IV: Rolling noise. *Journal of Sound and Vibration*, 46(3):419–436, 1976.

[51] P.J. Remington. Wheel/rail rolling noise, I: Theoretical analysis. *Journal of the Acoustical Society of America*, 81(6):1824–1832, 1987.

[52] P.J. Remington. Wheel/rail rolling noise, II: Validation of the theory. *Journal of the Acoustical Society of America*, 81(6):1824–1832, 1987.

[53] H. Reusner. *Druckflächenbelastung und Oberflächenverschiebung im Wälzkontakt von Rotationskörpern*. PhD Thesis. TU Karlsruhe, 1977.

[54] W. Scholl. Schwingungsuntersuchungen an Eisenbahnschienen. *Acustica*, 52(1):10–15, 1982.

[55] A. Sladkowski and M. Sitarz. Analysis of wheel/rail interaction using FE software. *Wear*, 258:1217–1223, 2005.

[56] E. Tassilly and N. Vincent. A linear model for the corrugation of rails. *Journal of Sound and Vibration*, 150(1):25–45, 1991.

[57] T. Telliskivi and U. Olofsson. Contact mechanics analysis of measured wheel-rail profiles using the finite element method. *Proc IMechE, Part F: Journal of Rail and Rapid Transport*, 215:65–72, 2001.

[58] D.J. Thompson. Wheel-rail noise generation, Part I: Introduction and interaction model. *Journal of Sound and Vibration*, 161(3):387–400, 1993.

[59] D.J. Thompson. Wheel-rail noise generation, Part II: Wheel vibration. *Journal of Sound and Vibration*, 161(3):401–419, 1993.

[60] D.J. Thompson. Wheel-rail noise generation, Part III: Rail vibration. *Journal of Sound and Vibration*, 161(3):421–446, 1993.

[61] D.J. Thompson. Wheel-rail noise generation, Part IV: Contact zone and results. *Journal of Sound and Vibration*, 161(3):447–466, 1993.

[62] D.J. Thompson. Wheel-rail noise generation, Part V: Inclusion of wheel rotation. *Journal of Sound and Vibration*, 161(3):467–482, 1993.

[63] D.J. Thompson. On the relationship between wheel and rail surface roughness and rolling noise. *Journal of Sound and Vibration*, 193(1):149–160, 1996.

[64] D.J. Thompson. The influence of the contact zone on the excitation of wheel/rail noise. *Journal of Sound and Vibration*, 267:523–535, 2003.

[65] D.J. Thompson and P.-E. Gautier. Review of research into wheel/rail rolling noise reduction. *Proc IMechE, Part F: Journal of Rail and Rapid Transport*, 220(4):385–408, 2006.

[66] D.J. Thompson, B. Hemsworth, and N. Vincent. Experimental validation of the TWINS prediction program for rolling noise, part 1: Description of the model and method. *Journal of Sound and Vibration*, 193(1):123–135, 1996.

[67] D.J. Thompson and C.J.C. Jones. A review of the modelling of wheel/rail noise generation. *Journal of Sound and Vibration*, 231(3):519–536, 2000.

[68] D.J. Thompson and N. Vincent. Track dynamic behaviour at high frequencies. Part 1: Theoretical models and laboratory measurements. *Vehicle System Dynamics*, Supplement 24:86–99, 1995.

[69] N. Vincent and D.J. Thompson. Track dynamic behaviour at high frequencies. Part 2: Experimental results and comparisons with theory. *Vehicle System Dynamics*, Supplement 24:100–114, 1995.

[70] H. Wu and J.M. Wang. Non-Hertzian conformal contact at wheel/rail interface. In *Proceedings of the 1995 IEEE/ASME Joint Railroad Conference, April 4-6, 1995, Baltimore, Maryland*, pages 137–144. Institute of Electrical and Electronics Engineering, 1995.

[71] T.X. Wu and D.J. Thompson. Theoretical investigation of wheel/rail nonlinear interaction due to roughness excitation. *Vehicle System Dynamics*, 34:261–282, 2000.

[72] T.X. Wu and D.J. Thompson. A hybrid model for the noise generation due to railway wheel flats. *Journal of Sound and Vibration*, 251(1):115–139, 2002.

[73] T.X. Wu and D.J. Thompson. On the impact noise generation due to a wheel passing over rail joints. *Journal of Sound and Vibration*, 267:485–496, 2003.

[74] W. Yan and D. Fischer. Applicability of the Hertz contact theory to rail-wheel contact problems. *Archive of Applied Mechnics*, 255-268(70):255–268, 2000.